



Strong-form meshfree collocation method for multibody thermomechanical contact

Andrew Beel¹ · Jeong-Hoon Song¹ 

Received: 29 May 2021 / Accepted: 14 September 2021

© The Author(s), under exclusive licence to Springer-Verlag London Ltd., part of Springer Nature 2021

Abstract

This study presents a strong form-based meshfree point collocation method for thermomechanical contact between two deformable bodies. The proposed method, based on Taylor approximation and the method of moving least squares, is implemented in a staggered Newton–Raphson framework to directly discretize and solve the governing nonlinear system of partial differential equations. Following the formulation of the proposed method and the discretization of the governing equations, four numerical examples are presented to verify the computational framework described. The first two examples, involving frictional contact along an inclined surface and Hertzian contact between two half-cylinders, verify the method’s ability to simulate two-body mechanical contact. The next two examples, involving coupled mechanical and thermal contact between rectangular blocks for two loading conditions, verify the ability of the method to simulate thermomechanical contact.

Keywords Multibody contact · Thermo-mechanical interaction · Strong form · Meshfree · Collocation

1 Introduction

The mechanics of contact, particularly thermomechanical contact, has wide-ranging applications in engineering, from modeling automobile crash safety to hip joint replacements to pellet-cladding interactions in a nuclear fuel rod [1–3]. Due to the nonlinear dependence of the contact traction and heat flux on the displacement and temperature fields, the governing equations for thermomechanical contact are nonlinear. In many of the applications of thermomechanical contact, coupling between the mechanical and thermal fields is an important concern. For example, temperature changes may cause significant thermal expansion, mechanical friction may generate significant heat, and degree of heat transfer across contact surfaces may depend significantly on the contact pressure [1, 4]. These applications and concerns have motivated the development of computational methods for solving contact problems numerically.

In the majority of computational studies of contact problems, the finite-element method (FEM) has been used. In

particular, these studies have involved special techniques to model contact interfaces and handle associated constraints. For example, Papadopoulos and Taylor [5] developed a mixed finite-element method for contact problems. Wriggers and Miehe [6] developed a finite-element method for large deformation thermomechanical contact. Another popular approach to solving contact problems is the mortar finite-element method, inspired by techniques for domain decomposition in the context of parallel computing. This method was developed and used, for example, in [7] and used in [8–13] for various contact problems. Despite considerable success, FEM approaches have been known to suffer from high computational cost due to mesh dependency and numerical integration [14]. FEM approaches also have difficulty with adaptive mesh refinement, which is frequently required to resolve the contact interface. Such refinement is required because of sharp gradients observed near transitions between stick and slip conditions and near the edges of contact interfaces. Another challenge for FEM approaches is that special techniques must be developed to overcome the possibility of element node-to-segment contact [1].

To combat these issues, a strong form-based meshfree point collocation method is proposed in this study as an alternative or supplement to the FEM for contact problems. The proposed method, based on Taylor approximation and moving least squares (MLS), was first developed in [15–20].

✉ Jeong-Hoon Song
jh.song@colorado.edu

¹ Department of Civil, Environmental and Architectural Engineering, University of Colorado, Boulder, CO 80309, USA

By directly discretizing the strong form of governing PDEs using a set of approximate derivative operators, the proposed method avoids mesh dependency, domain integration, and exact computation of derivatives [14]. In addition, the proposed method easily treats boundary conditions and adaptive refinement. Motivated by these advantages, the method has been successfully applied to various problems, including incompressible fluid flows [19], elastic crack problems [21], and the asymptotic crack tip singularity in a linear elastic fracture [22, 23]. Later, the method was applied to weak and strong discontinuities [14, 24–26], diffusive interface modeling and stress analysis [27–29], inelastic material problems [30], frictional contact [31], and wind-driven ocean circulation [32].

It should be noted that the proposed method is only one of many recently developed collocation methods. Other examples include the reproducing kernel collocation method [33, 34] and the isogeometric analysis collocation (IGA-C) method [35, 36]. Only the IGA-C method has been for contact problems [35], as well as large deformation elasticity [36] and rod-to-rod contact [37]. However, as explained in [35], the IGA-C method employs tensor product or locally refined meshes, and therefore, is not meshfree. In contrast to these previous studies, this study verifies the proposed meshfree, strong form-based collocation framework for multibody and thermomechanical contact problems through a set of benchmark problems.

Irrespective of the numerical method used to solve the governing PDEs, one of two general approaches is used to simulate thermomechanical contact in a computational context. These are the staggered (loose coupling) and monolithic (tight coupling) iterative approaches. In each step of a staggered scheme, the displacement and temperature fields are assumed to be fixed with respect to each other, and both fields are adjusted individually in a fixed-point iteration until both converge. In contrast, a monolithic scheme considers all interactions between thermal and mechanical fields within one iteration and solves one system of equations that includes all solution variables [38]. In general, a staggered approach is more likely to be successful if displacement due to thermal expansion is expected to be small compared to displacement due to mechanical loading. In contrast, a monolithic scheme would be more appropriate when thermal expansion is significant. Other researchers have explored both monolithic and staggered approaches for thermoelasticity and thermomechanical contact problems. For example, a monolithic approach was used in [39] to model thermo-structure interaction and applied to examples related to behavior of rocket nozzles. In [40], an unconditionally stable staggered scheme was developed for use in time-dependent thermoelasticity problems. In this study, a staggered Newton–Raphson scheme is used because the

mechanical and thermal fields are loosely coupled for the problems considered here.

In summary, this study introduces a computational framework for solving problems in multibody thermomechanical contact using a strong-form meshfree collocation method. The outline of this paper is as follows. First, Sect. 2 describes the equations that govern multibody thermomechanical contact, including the contact constraints that introduce nonlinearity into the problem. Section 3 reviews the formulation of the proposed method. Section 4 explains how the strong forms of the governing equations are discretized using the proposed method and how these discretized equations are solved using a staggered Newton–Raphson scheme. Section 5 provides four verification examples for the proposed computational framework. The first two examples involve frictional contact along an inclined interface and Hertzian contact between two half-cylinders, which verify the method for multibody contact problems. The final two examples involve contact between two rectangular blocks under different loading conditions, which verify the proposed method for thermomechanical contact. Finally, conclusions are given in Sect. 6.

2 Equations for thermomechanical contact

In this section, the governing equations for thermomechanical contact are developed. First, an overview of the geometry, interior domain equations, and boundary conditions are given. Next, the mechanical contact constraints are described and regularized using a penalty approach. Finally, the thermal contact model is introduced.

2.1 Geometry, governing equations, and boundary conditions

This study concerns loosely coupled thermomechanical contact between two deformable bodies in two dimensions, the interiors of which are denoted by Ω^1 and Ω^2 , as shown in Fig. 1. For $\alpha \in \{1, 2\}$, the closure of the domain Ω^α is denoted by $\bar{\Omega}^\alpha$, i.e., $\bar{\Omega}^\alpha = \Omega^\alpha \cup \Gamma^\alpha$, where Γ^α is the entire boundary of the domain Ω^α . Each total boundary Γ^α is partitioned such that $\Gamma^\alpha = \Gamma_u^\alpha \cup \Gamma_t^\alpha \cup \Gamma_c^\alpha$ with $\Gamma_u^\alpha \cap \Gamma_t^\alpha = \Gamma_u^\alpha \cap \Gamma_c^\alpha = \Gamma_c^\alpha \cap \Gamma_t^\alpha = \emptyset$. Here, Γ_u^α denotes the subset of the boundary of Ω^α on which displacement \mathbf{u} is prescribed, Γ_t^α the subset on which traction is prescribed, and Γ_c^α the subset on which contact between the two bodies is expected to occur. Each total boundary Γ^α is simultaneously partitioned in terms of temperature-related boundary conditions such that $\Gamma^\alpha = \Gamma_\theta^\alpha \cup \Gamma_q^\alpha \cup \Gamma_c^\alpha$ with $\Gamma_\theta^\alpha \cap \Gamma_q^\alpha = \Gamma_\theta^\alpha \cap \Gamma_c^\alpha = \Gamma_c^\alpha \cap \Gamma_q^\alpha = \emptyset$. Here, Γ_θ^α denotes the subset of the boundary of Ω^α on which temperature θ is prescribed and Γ_q^α the subset on which normal heat flux is prescribed. Finally, $\bar{\Omega} = \bar{\Omega}^1 \cup \bar{\Omega}^2$ is used to denote the entire domain of

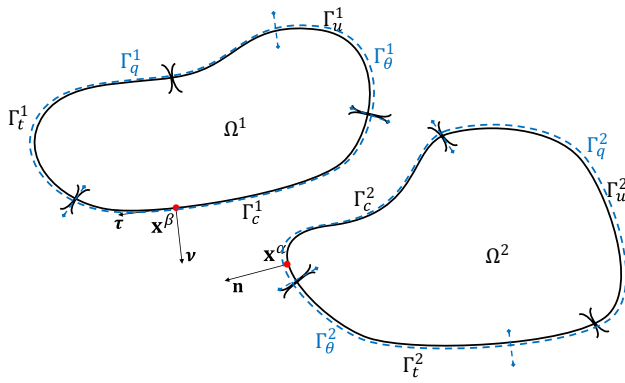


Fig. 1 Notation for two-body contact

interest, namely the set of all points in either of the two bodies or their boundaries; $\Omega = \Omega^1 \cup \Omega^2$ denotes the interior thereof.

The objective in this study is to find the displacement \mathbf{u} and change in temperature θ (from some reference temperature θ_0) over Ω that satisfy mechanical equilibrium and thermal equilibrium subject to boundary conditions. The equations for mechanical equilibrium are given by

$$\nabla \cdot \boldsymbol{\sigma} + \mathbf{b} = 0 \quad \text{in } \Omega. \quad (2.1)$$

Here, $\boldsymbol{\sigma}$ is the Cauchy stress tensor and \mathbf{b} is a body force. Although the two bodies are permitted to have different material properties, they are assumed to be homogeneous, linear thermoelastic and isotropic. Thus, the appropriate constitutive equation is

$$\boldsymbol{\sigma} = 2\mu(\boldsymbol{\epsilon} - \boldsymbol{\epsilon}^\theta) + \lambda \text{tr}(\boldsymbol{\epsilon} - \boldsymbol{\epsilon}^\theta) \mathbf{1}. \quad (2.2)$$

In (2.2), λ and μ are Lamé constants, $\mathbf{1}$ is the second-order identity tensor, and $\boldsymbol{\epsilon}$ is the mechanical strain tensor, and $\boldsymbol{\epsilon}^\theta$ is the thermal strain tensor. Small displacement and strain are assumed, so the mechanical strain is defined by

$$\boldsymbol{\epsilon} = \frac{1}{2}(\nabla \mathbf{u} + (\nabla \mathbf{u})^T). \quad (2.3)$$

The thermal strain is related to the temperature change by

$$\boldsymbol{\epsilon}^\theta = \alpha_v \theta \mathbf{1}. \quad (2.4)$$

The constant α_v in (2.4) is the coefficient of thermal expansion.

The equations for thermal equilibrium are given by

$$\nabla \cdot \mathbf{q} + s = 0. \quad (2.5)$$

Here, \mathbf{q} is heat flux and s is a heat source. The heat flux is assumed to be proportional to the temperature gradient according to Fourier's Law:

$$\mathbf{q} = -\kappa \nabla \theta. \quad (2.6)$$

The constant κ in (2.6) is the thermal conductivity.

Which fields \mathbf{u} and θ satisfy the equations above depend on the boundary conditions. The field \mathbf{u} at each point on the boundary Γ is subject to one (or a mix) of the following conditions:

$$\begin{aligned} \mathbf{u} &= \bar{\mathbf{u}} & \text{on } \Gamma_u^\alpha, \\ \boldsymbol{\sigma} \mathbf{n} &= \bar{\mathbf{t}} & \text{on } \Gamma_t^\alpha, \\ \boldsymbol{\sigma} \mathbf{n} &= \mathbf{t}^c & \text{on } \Gamma_c^\alpha, \end{aligned} \quad (2.7)$$

for each $\alpha \in \{1, 2\}$. In (2.7), \mathbf{n} is the unit outward normal vector to Ω , $\bar{\mathbf{u}}$ is the prescribed displacement on Γ_u^α , $\bar{\mathbf{t}}$ is the prescribed traction on Γ_t^α , and \mathbf{t}^c is the contact traction on Γ_c^α which is determined based on the formulation in subsequent sections. The field θ at each point on the boundary is subject to one of the following conditions:

$$\begin{aligned} \theta &= \bar{\theta} & \text{on } \Gamma_\theta^\alpha, \\ \mathbf{q} \cdot \mathbf{n} &= \bar{q} & \text{on } \Gamma_q^\alpha, \\ \mathbf{q} \cdot \mathbf{n} &= q^c & \text{on } \Gamma_c^\alpha. \end{aligned} \quad (2.8)$$

In (2.8), $\bar{\theta}$ is the prescribed temperature change on Γ_θ^α , \bar{q} is the prescribed normal heat flux on Γ_q^α , and q^c is the normal heat flux across the contact surface Γ_c^α .

The following sections describe the contact constraints that govern the interaction between $\bar{\Omega}^1$ and $\bar{\Omega}^2$. Some basic assumptions motivate the formulation presented here. First, at this length scale, it is assumed that there is no interpenetration between the two bodies during contact (although this assumption is relaxed during the penalty regularization of the normal contact constraint). Second, it is assumed that any force exerted on one body by the other is compressive, i.e., no cohesion exists between the bodies. Coulomb friction is assumed between the bodies, controlled by a coefficient of friction μ_f . Finally, it is assumed that the heat flux across the contact interface is strictly conductive and depends on the contact pressure at the interface.

2.2 Normal and frictional contact constraints

First, we must define quantities associated with two points potentially in contact. Since both bodies subject to contact are deformable, the contact traction at a point $\mathbf{x}^\alpha \in \Gamma_c^\alpha$ will depend on the relative displacement between \mathbf{x}^α and the corresponding point $\mathbf{x}^\beta(\mathbf{x}^\alpha) \in \Gamma_c^\beta$ with which \mathbf{x}^α is potentially in contact. For each pair of corresponding contact points, a vector $\mathbf{n}(\mathbf{x}^\alpha)$ is used to denote the outward unit normal to Γ_c^α at \mathbf{x}^α , while $\mathbf{v}(\mathbf{x}^\alpha) = \mathbf{n}(\mathbf{x}^\beta)$ is used to denote the outward unit normal to Γ_c^β at \mathbf{x}^β . The vector $\boldsymbol{\tau}(\mathbf{x}^\beta)$ denotes the unit tangent to Γ_c^β at \mathbf{x}^β . Specifically, this unit tangent is defined by

$$\boldsymbol{\tau} = \boldsymbol{\nu} \times \mathbf{e}_3, \quad (2.9)$$

where \mathbf{e}_3 is the unit basis vector pointing out of the paper. It is convenient to decompose the contact traction \mathbf{t}^c at a point \mathbf{x} into components along $\boldsymbol{\nu}$ and $\boldsymbol{\tau}$, as follows:

$$\mathbf{t}^c = \mathbf{t}_N - \mathbf{t}_T = t_N \boldsymbol{\nu} - t_T \boldsymbol{\tau}. \quad (2.10)$$

For a more detailed discussion of these definitions, the reader is referred to Laursen's book [41].

Next, given a displacement field $\mathbf{u} : \Gamma_c^1 \cup \Gamma_c^2 \rightarrow \mathbb{R}^2$, we define a so-called gap function $g : \Gamma_c^1 \cup \Gamma_c^2 \rightarrow \mathbb{R}$ in terms of the relative displacement between a point on Γ^α and the corresponding contact point on Γ^β . Roughly speaking, the gap function represents the component of the vector between corresponding contact points in the deformed configuration normal to one of the contact surfaces. For all $\mathbf{x}^\alpha \in \Gamma_c^\alpha$ and $\mathbf{x}^\beta(\mathbf{x}^\alpha) \in \Gamma_c^\beta$,

$$g(\mathbf{x}^\alpha) = g_0(\mathbf{x}^\alpha) - [\mathbf{u}(\mathbf{x}^\alpha) - \mathbf{u}(\mathbf{x}^\beta(\mathbf{x}^\alpha))] \cdot \boldsymbol{\nu}(\mathbf{x}^\alpha), \quad (2.11)$$

where $g_0(\mathbf{x}^\alpha) = -[\mathbf{x}^\alpha - \mathbf{x}^\beta(\mathbf{x}^\alpha)] \cdot \boldsymbol{\nu}(\mathbf{x}^\alpha)$ denotes the initial gap between the two bodies.

Based on the assumptions outlined at the beginning of this section, the gap function g and contact pressure t_N are related through the Kuhn–Tucker complementary conditions:

$$g \leq 0, \quad t_N \geq 0, \quad t_N g = 0. \quad (2.12)$$

Equation (2.12)₁ reflects the impenetrability of the bodies. Equation (2.12)₂ reflects the solely compressive nature of the contact pressure. Equation (2.12)₃ reflects that contact pressure is nonzero only if the gap between two points is closed and the two points are separated only if the contact pressure is zero.

The tangential component of the contact traction is governed by Coulomb friction. In other words, the tangential traction may not exceed $\mu_f t_N$ in magnitude. If t_T reaches $\mu_f t_N$ between two contact points, then the points will begin to displace relative to each other along the tangential direction (slip condition). Short of this, however, there will be no relative tangential displacement between the points (stick condition). Introducing the following definitions will help express these frictional constraints symbolically. Let the relative tangential displacement between two contact points be denoted by

$$\boldsymbol{\psi}(\mathbf{x}^\alpha) := [\mathbf{u}(\mathbf{x}^\alpha) - \mathbf{u}(\mathbf{x}^\beta(\mathbf{x}^\alpha))] \cdot \boldsymbol{\tau}(\mathbf{x}^\beta(\mathbf{x}^\alpha)). \quad (2.13)$$

Let the difference between the tangential traction magnitude and its upper limit, called the trial function, be denoted by

$$\Phi := |t_T| - \mu_f t_N. \quad (2.14)$$

With these definitions, the friction constraints may be expressed as follows:

$$\Phi \leq 0, \quad \text{sign}(\boldsymbol{\psi}) = \text{sign}(t_T), \quad \Phi \boldsymbol{\psi} = 0. \quad (2.15)$$

Equation (2.15)₁ reflects the friction limit on the magnitude of the tangential traction. Equation (2.15)₂ reflects that the direction of the tangential traction vector is opposite the relative displacement after taking into account the convention used for $\boldsymbol{\tau}$. Equation (2.15)₃ reflects that relative tangential displacement between two corresponding contact points can be nonzero only if the magnitude of the tangential traction has reached its Coulomb friction limit as a function of the normal traction; conversely, the tangential traction has not reached its friction limit unless the relative tangential displacement is nonzero.

2.3 Penalty regularization of mechanical contact constraints

To simplify the numerical solution of such contact problems, the Kuhn–Tucker conditions (2.12) and (2.15) are relaxed by introducing a penalty regularization of the normal and frictional contact constraints. To regularize the normal contact constraint, the normal contact pressure is assumed to vary sharply linearly with the normal component of the interpenetration between the two bodies:

$$t_N = \epsilon_N \langle g \rangle. \quad (2.16)$$

Here, ϵ_N is the normal penalty parameter (chosen to be a few orders of magnitude higher than the stiffness of the bodies), g is the familiar gap function, and $\langle \cdot \rangle$ is the Macaulay bracket defined by

$$\langle g \rangle = \begin{cases} g & \text{if } g \geq 0, \\ 0 & \text{otherwise.} \end{cases} \quad (2.17)$$

To regularize the frictional contact constraint, the tangential traction under the stick condition is assumed to vary sharply linearly with the relative tangential displacement:

$$t_T^{\text{stick}} = \epsilon_T \boldsymbol{\psi}. \quad (2.18)$$

Here, ϵ_T is the tangential penalty parameter (also chosen to be a few orders of magnitude higher than the stiffness of the bodies).

Whether two corresponding contact points are under the stick or slip condition is determined from the trial state/return mapping algorithm, outlined as follows. First, the stick condition is assumed as the *trial state*, and the trial

function (2.14) is computed based on the normal traction from (2.16) and the trial state tangential traction from (2.18). If the trial function is positive, the stick assumption is determined to be incorrect. Thus, in the *return mapping*, the tangential traction is equated to its friction limit. In summary, the trial state/return algorithm based on the regularized contact constraints proceeds as follows:

1. Compute the trial state, assuming the stick condition:

$$\begin{aligned} t_N &= \epsilon_N \langle g \rangle, \\ t_T^{\text{trial}} &= \epsilon_T \psi, \\ \Phi^{\text{trial}} &= |t_T^{\text{trial}}| - \mu_f t_N. \end{aligned} \quad (2.19)$$

2. Check the slip condition:

$$t_T = \begin{cases} t_T^{\text{trial}} & \text{if } \Phi^{\text{trial}} \leq 0 \text{ (stick),} \\ \mu_f t_N \text{sign}(\psi) & \text{otherwise (slip).} \end{cases} \quad (2.20)$$

The regularizations of the normal and frictional contact constraints are represented graphically in Fig. 2.

2.4 Thermal contact constraint

The heat flux across the contact interface is assumed to be conductive and to depend on both the contact pressure and the temperature jump between the two bodies at the interface. Based on these assumptions, the following empirical law suggested by Ref. [4] is introduced for the normal heat flux due to contact between $\mathbf{x}^\alpha \in \Gamma_c^\alpha$ and $\mathbf{x}^\beta \in \Gamma_c^\beta$:

$$q^c(\mathbf{x}^\alpha) = h(t_N) [\theta(\mathbf{x}^\alpha) - \theta(\mathbf{x}^\beta(\mathbf{x}^\alpha))]. \quad (2.21)$$

Here, $h(t_N)$ is the pressure-dependent conductivity across the interface. This conductivity is determined using the empirical power law:

$$h(t_N) = h_0 \left(\frac{t_N}{H_e} \right)^P. \quad (2.22)$$

In (2.22), h_0 is a reference conductivity determined experimentally, P is an exponent determined experimentally, and H_e is the Vickers hardness. The contact pressure t_N is determined from (2.16).

3 Strong-form meshfree collocation method

This section summarizes the formulation of the proposed strong-form meshfree collocation method and explains its implementation in a staggered Newton–Raphson framework in the context of thermomechanical contact.

3.1 Formulation of the proposed method

The proposed method is based on Taylor approximation and the method of moving least squares. A function $u(\mathbf{x})$ in n_{dim} spatial dimensions with $\mathbf{x} = \{x_1, x_2, \dots, x_{n_{\text{dim}}}\}$ may be approximated by an m^{th} order Taylor series:

$$u(\mathbf{x}) = \sum_{|\alpha| \leq m} \frac{D^\alpha u(\bar{\mathbf{x}})}{\alpha!} (\mathbf{x} - \bar{\mathbf{x}})^\alpha + H.O.T. \quad (3.1)$$

Here, $\bar{\mathbf{x}}$ is a local center and α is an array of n_{dim} nonnegative integers. Some notation involving α is defined as follows:

$$|\alpha| := \sum_{k=1}^{n_{\text{dim}}} \alpha_k \quad \alpha! := \prod_{k=1}^{n_{\text{dim}}} \alpha_k! \quad \mathbf{x}^\alpha := \prod_{k=1}^{n_{\text{dim}}} x_k^{\alpha_k}. \quad (3.2)$$

Finally, $D^\alpha u(\bar{\mathbf{x}})$ denotes the α^{th} partial derivative of u evaluated at $\bar{\mathbf{x}}$, e.g., $D^{(1,2)} u(\bar{\mathbf{x}}) = \frac{\partial^2 u(\bar{\mathbf{x}})}{\partial x_1 \partial x_2}$. The series approximation (3.1) may be written as

$$\sum_{|\alpha| \leq m} \frac{D^\alpha u(\bar{\mathbf{x}})}{\alpha!} (\mathbf{x} - \bar{\mathbf{x}})^\alpha = \mathbf{p}^T(\mathbf{x}; \bar{\mathbf{x}}) \mathbf{a}(\bar{\mathbf{x}}). \quad (3.3)$$

Here, the sum of terms over $|\alpha| \leq m$ is written as the dot product of a polynomial basis vector \mathbf{p} and a derivative coefficient vector \mathbf{a} :

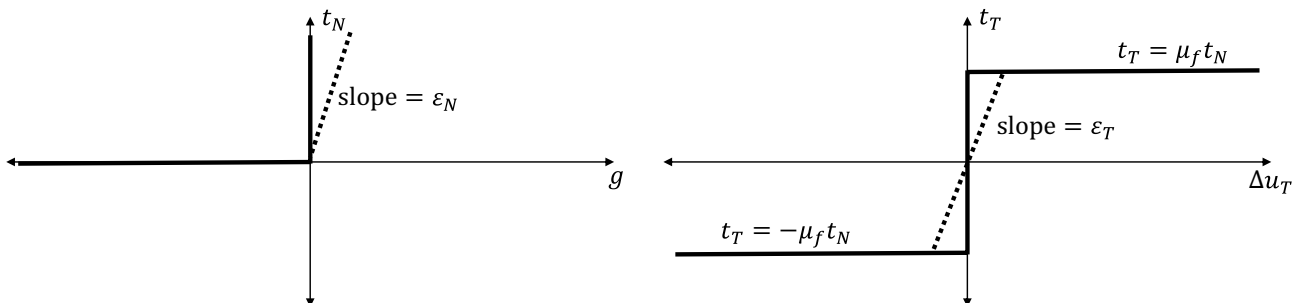


Fig. 2 Penalty regularization of normal (left) and frictional (right) contact constraints. Solid lines represent the strict Kuhn–Tucker constraints, while dotted lines represent the regularized constraints

$$\mathbf{p}(\mathbf{x};\bar{\mathbf{x}}) := \left\{ \frac{(\mathbf{x} - \bar{\mathbf{x}})^{\alpha_1}}{\alpha_1!}, \frac{(\mathbf{x} - \bar{\mathbf{x}})^{\alpha_2}}{\alpha_2!}, \dots, \frac{(\mathbf{x} - \bar{\mathbf{x}})^{\alpha_{L_p}}}{\alpha_{L_p}!} \right\}^T \quad (3.4)$$

$$\mathbf{a}(\bar{\mathbf{x}}) := \{D^{\alpha_1}u(\bar{\mathbf{x}}), D^{\alpha_2}u(\bar{\mathbf{x}}), \dots, D^{\alpha_{L_p}}u(\bar{\mathbf{x}})\}^T.$$

The length of \mathbf{p} and \mathbf{a} is $L_p = \frac{(n_{\text{dim}}+m)!}{n_{\text{dim}}!m!}$. The integer arrays $\alpha_1, \dots, \alpha_{L_p}$ are in lexicographical order by convention.

Now, consider a set of N collocation points on a domain Ω . If the value of u is known only at each of these N points, the vector \mathbf{a} of derivative coefficients must be found approximately. The best vector \mathbf{a} in the weighted least squares sense is found by minimizing the functional

$$\mathcal{F}[\mathbf{a}] = \sum_{j=1}^N w \left(\frac{\mathbf{x}_j - \bar{\mathbf{x}}}{\rho(\bar{\mathbf{x}})} \right) [\mathbf{p}(\mathbf{x}_j; \bar{\mathbf{x}})^T \mathbf{a}(\bar{\mathbf{x}}) - u(\mathbf{x}_j)]^2. \quad (3.5)$$

Here, w is a weight function with a compact support, i.e., positive inside and zero outside of a closed disk of radius $\rho(\bar{\mathbf{x}})$ surrounding $\bar{\mathbf{x}}$. The radius ρ , called the dilation parameter, may vary with the location of the local center over the domain Ω to adjust for spatial variation in the density and pattern of collocation points. Differentiating \mathcal{F} with respect to \mathbf{a} and setting the result equal to zero yields the optimal approximate derivative coefficient vector \mathbf{a}^* , given by

$$\mathbf{a}^*(\bar{\mathbf{x}}) = \mathbf{M}^{-1}(\bar{\mathbf{x}})\mathbf{B}(\bar{\mathbf{x}}). \quad (3.6)$$

Here, the matrix \mathbf{M} is given by

$$\mathbf{M}(\bar{\mathbf{x}}) = \sum_{j=1}^N w \left(\frac{\mathbf{x}_j - \bar{\mathbf{x}}}{\rho(\bar{\mathbf{x}})} \right) \mathbf{p}(\mathbf{x}_j; \bar{\mathbf{x}}) \mathbf{p}(\mathbf{x}_j; \bar{\mathbf{x}})^T. \quad (3.7)$$

The matrix \mathbf{B} is given by

$$\mathbf{B}(\bar{\mathbf{x}}) = \begin{bmatrix} w \left(\frac{\mathbf{x}_1 - \bar{\mathbf{x}}}{\rho(\bar{\mathbf{x}})} \right) \mathbf{p}(\mathbf{x}_1; \bar{\mathbf{x}}), & w \left(\frac{\mathbf{x}_2 - \bar{\mathbf{x}}}{\rho(\bar{\mathbf{x}})} \right) \mathbf{p}(\mathbf{x}_2; \bar{\mathbf{x}}), \\ \dots, & w \left(\frac{\mathbf{x}_N - \bar{\mathbf{x}}}{\rho(\bar{\mathbf{x}})} \right) \mathbf{p}(\mathbf{x}_N; \bar{\mathbf{x}}) \end{bmatrix}. \quad (3.8)$$

Note that the weight function w is not differentiated in this formulation, so non-smooth weight functions may be used.

For a single local center $\bar{\mathbf{x}}$, the approximate derivative vector \mathbf{a}^* minimizes the weighted least square residual globally. However, a best local approximation at each collocation point may be found by moving the local center to each collocation point \mathbf{x}_j , hence the term “moving least squares.” Thus, taking $\bar{\mathbf{x}} \rightarrow \mathbf{x}_j$, the best \mathbf{a} in the moving least squares sense at each collocation point \mathbf{x}_j is given by

$$\mathbf{a}(\mathbf{x}_j) = \mathbf{M}(\mathbf{x}_j)^{-1} \mathbf{B}(\mathbf{x}_j). \quad (3.9)$$

Since the α^{th} entry of $\mathbf{a}(\mathbf{x}_j)$ is an approximation for the α^{th} derivative of u evaluated at \mathbf{x}_j , the corresponding row of $\mathbf{M}(\mathbf{x}_j)^{-1} \mathbf{B}(\mathbf{x}_j)$ represents an approximate derivative operator.

Let $u^h(\mathbf{x}_j)$ denote the J^{th} discrete solution ordinate and define Φ_{JJ}^{α} to be the J^{th} entry of the α^{th} row of $\mathbf{M}(\mathbf{x}_j)^{-1} \mathbf{B}(\mathbf{x}_j)$. Then, an approximation for the α^{th} derivative of u evaluated at \mathbf{x}_j is given by

$$D^{\alpha}u(\mathbf{x}_j) \approx \sum_{J=1}^N \Phi_{JJ}^{\alpha} u^h(\mathbf{x}_j). \quad (3.10)$$

Thus, the strong form of a PDE may be directly discretized by replacing exact derivative expressions with expressions of the form (3.10).

3.2 Staggered Newton–Raphson scheme

Any nonlinear system of equations may be written as

$$\mathbf{R}(\mathbf{u}) = \mathbf{y}(\mathbf{u}) - \mathbf{f} = \mathbf{0}. \quad (3.11)$$

Here, \mathbf{R} , called the residual, is a nonlinear mapping of the solution vector \mathbf{u} . The terms \mathbf{y} and \mathbf{f} are the non-constant and constant parts of \mathbf{R} , respectively. The traditional Newton–Raphson (NR) technique for finding the root \mathbf{u} of this equation is defined by the iterative scheme

$$\mathbf{u}_{k+1} = \mathbf{u}_k - \mathbf{K}_k^{-1} \mathbf{R}(\mathbf{u}_k). \quad (3.12)$$

Of course, an initial guess \mathbf{u}_0 is required to begin the iteration. In (3.12), k denotes the iteration step and \mathbf{K} , called the tangent stiffness matrix, is defined on the k th step by

$$\mathbf{K} := \frac{\partial \mathbf{R}(\mathbf{u}_k)}{\partial \mathbf{u}}. \quad (3.13)$$

It is convenient to denote the update term in (3.12) by

$$\delta \mathbf{u}_k := -\mathbf{K}^{-1} \mathbf{R}(\mathbf{u}_k). \quad (3.14)$$

The iteration in (3.12) is repeated until a desired stopping criterion is reached. A commonly used stopping criterion based on the magnitude of the solution vector update is

$$\text{IF } \frac{\|\delta \mathbf{u}_k\|}{\|\mathbf{u}_k - \mathbf{u}_0\|} < \text{TOL}, \quad \text{THEN Stop NR loop.} \quad (3.15)$$

Another commonly used stopping criterion based on the magnitude of the residual is

$$\text{IF } \frac{\|\mathbf{R}_k\|}{\|\mathbf{R}_0\|} < \text{TOL}, \quad \text{THEN Stop NR loop.} \quad (3.16)$$

In the context of the present study, the nonlinear system of interest consists of the strong forms of both the mechanical and thermal governing equations, boundary conditions, and contact constraints discretized directly at the collocation points. There are two separate solution vectors in this system. The first is the nodal displacement solution vector given by

$$\mathbf{U} = \begin{bmatrix} u_1^h(\mathbf{x}_1) \\ u_2^h(\mathbf{x}_1) \\ u_1^h(\mathbf{x}_2) \\ u_2^h(\mathbf{x}_2) \\ \vdots \\ u_1^h(\mathbf{x}_N) \\ u_2^h(\mathbf{x}_N) \end{bmatrix}. \quad (3.17)$$

The second solution vector is the nodal temperature change vector, given by

$$\mathbf{T} = \begin{bmatrix} \theta^h(\mathbf{x}_1) \\ \theta^h(\mathbf{x}_2) \\ \vdots \\ \theta^h(\mathbf{x}_N) \end{bmatrix}. \quad (3.18)$$

Here, \mathbf{x}_i is the i th collocation point, N is the total number of collocation points, u_i^h corresponds to the i th displacement degree of freedom, and T^h corresponds to the temperature change. In the present study, there are a total of three degrees of freedom, namely the x - and y -components of displacement and temperature change. For convenience, $\mathbf{U}_i := \{u_i^h(\mathbf{x}_1), \dots, u_i^h(\mathbf{x}_N)\}^T$ will be used to denote the separated solution vectors for the two degrees of freedom.

Unlike conventional meshfree method [42], the numerical difficulty associated with lacking Kronecker-delta property has been circumvented in this method. Thus, the direct nodal solutions \mathbf{U} and \mathbf{T} may have quite good accuracy without a reinterpolation procedure. However, to further ensure accuracy of the method, nodal solution \mathbf{u} is reinterpolated with the $(0, 0)$ differential operator:

$$u_i(\mathbf{x}_i) \approx \Phi_i^{(0,0)} \mathbf{U}_i. \quad (3.19)$$

Similarly, temperature change at the nodes is also reinterpolated according to

$$\theta(\mathbf{x}_i) \approx \Phi_i^{(0,0)} \mathbf{T}. \quad (3.20)$$

Note that more rigorous numerical studies investigating the effects of the direct use of nodal solution to the accuracy remain a future work.

With this iterative solution framework, the proposed strong-form collocation method may be used to determine the appropriate tangent stiffness matrices \mathbf{K}_U and \mathbf{K}_T and residual vectors \mathbf{R}_U and \mathbf{R}_T for the two-body thermomechanical contact problem. Using these matrices and vectors, the staggered Newton–Raphson scheme outlined below may be used to determine the solution vectors \mathbf{U} and \mathbf{T} :

Staggered Newton–Raphson scheme for thermomechanical contact

1. Compute residual vector \mathbf{R}_U and tangent stiffness matrix \mathbf{K}_U using \mathbf{U} and \mathbf{T} from previous iteration.

2. Compute update $\delta \mathbf{U}$ from (3.14) using \mathbf{R}_U and \mathbf{K}_U . Update \mathbf{U} according to (3.12).
3. Compute residual vector \mathbf{R}_T and tangent stiffness matrix \mathbf{K}_T using updated \mathbf{U} .
4. Compute update $\delta \mathbf{T}$ from (3.14) using \mathbf{R}_T and \mathbf{K}_T . Update \mathbf{T} according to (3.12).
5. Check convergence criteria [e.g., (3.15) or (3.16)] separately for \mathbf{U} and \mathbf{T} .
6. Repeat steps 1–5 until both convergence criteria are satisfied.

4 Discretization of governing equations

The strong-form collocation method may be employed in a staggered Newton–Raphson framework to solve the non-linear problem represented by the governing equations presented in Sect. 2 with the regularized contact constraints from Sect. 2. In this section, the governing equations are discretized and placed in the Newton–Raphson framework. The discussion begins with the equations of mechanical equilibrium and non-contact boundary conditions, followed by the mechanical contact constraints, and ending with the thermal equations.

4.1 Discretization of mechanical equilibrium and boundary conditions

To determine the discrete form of the equilibrium Eqs. (2.1), the constitutive Eq. (2.2), and the strain-displacement Eqs. (2.3) and (2.4) are substituted in (2.1) to yield

$$\mu \Delta \mathbf{u} + (\lambda + \mu) \nabla (\nabla \cdot \mathbf{u}) - 2\alpha'_v (\lambda + \mu) \nabla \theta + \mathbf{b} = 0 \quad \text{in } \Omega. \quad (4.1)$$

Here, plane strain is assumed, so that the Lamé constants are given by

$$\lambda = \frac{\nu E}{(1 - 2\nu)(1 + \nu)}, \quad \mu = \frac{E}{2(1 + \nu)}, \quad (4.2)$$

where E is Young's modulus, and ν is Poisson's ratio (not to be confused with \mathbf{v} , the contact normal vector). Note that a modified plane strain coefficient of thermal expansion $\alpha'_v = (1 + \nu)\alpha_v$ is used in (4.1). In index notation for Cartesian components, (4.1) is written equivalently as

$$\mu u_{i,jj} + (\lambda + \mu) u_{j,ji} - 2\alpha'_v (\lambda + \mu) \theta_{,i} + b_i = 0 \quad \text{in } \Omega, \quad (4.3)$$

where $i, j = 1, 2$ in two dimensions and repeated indices obey the summation convention. When these equations are expanded explicitly, they become the pair of equations

$$\begin{aligned}
& (\lambda + 2\mu)u_{1,11} + \mu u_{1,22} + (\lambda + \mu)u_{2,21} \\
& - 2\alpha'_v(\lambda + \mu)\theta_{,1} + b_1 = 0 \\
& (\lambda + \mu)u_{1,12} + (\lambda + 2\mu)u_{2,22} + \mu u_{2,11} \\
& - 2\alpha'_v(\lambda + \mu)\theta_{,2} + b_2 = 0.
\end{aligned} \quad (4.4)$$

The strong form of the PDEs in (4.4) are discretized by replacing the various derivative terms with approximate derivatives constructed using the differential operators from Chapter 3. This discretization is used to construct the equations for each interior collocation point. Suppose $\mathbf{x}_I \in \Omega$ is an interior collocation point and let Φ_{IJ}^α represent the J th entry of the α^{th} differential operator at collocation point \mathbf{x}_I . Then, the equations in (4.4) for node $\mathbf{x}_I \in \Omega$ are discretized as

$$\begin{aligned}
R_{I1}^{\text{intU}} &:= \sum_{J=1}^N \left[\left((\lambda + 2\mu)\Phi_{IJ}^{(2,0)} + \mu\Phi_{IJ}^{(0,2)} \right) u_1^h(\mathbf{x}_J) \right. \\
&\quad \left. + \left((\lambda + \mu)\Phi_{IJ}^{(1,1)} \right) u_2^h(\mathbf{x}_J) \right] \\
&\quad - \sum_{J=1}^N \left(2\alpha'_v(\lambda + \mu)\Phi_{IJ}^{(1,0)} \right) \theta^h(\mathbf{x}_J) + b_1(\mathbf{x}_I) \\
R_{I2}^{\text{intU}} &:= \sum_{J=1}^N \left[\left((\lambda + \mu)\Phi_{IJ}^{(1,1)} \right) u_1^h(\mathbf{x}_J) + \left((\lambda + 2\mu)\Phi_{IJ}^{(0,2)} \right. \right. \\
&\quad \left. \left. + \mu\Phi_{IJ}^{(2,0)} \right) u_2^h(\mathbf{x}_J) \right] \\
&\quad - \sum_{J=1}^N \left(2\alpha'_v(\lambda + \mu)\Phi_{IJ}^{(0,1)} \right) \theta^h(\mathbf{x}_J) + b_2(\mathbf{x}_I).
\end{aligned} \quad (4.5)$$

Thus, for node $\mathbf{x}_I \in \Omega$, the 2×2 IJ block of \mathbf{K}_U is given by the partial derivative of (4.5) with respect to $\{u_1^h(\mathbf{x}_J), u_2^h(\mathbf{x}_J)\}$, i.e.,

$$\mathbf{K}_{IJ}^{\text{intU}} = \begin{bmatrix} (\lambda + 2\mu)\Phi_{IJ}^{(2,0)} + \mu\Phi_{IJ}^{(0,2)} & (\lambda + \mu)\Phi_{IJ}^{(1,1)} \\ (\lambda + \mu)\Phi_{IJ}^{(1,1)} & (\lambda + 2\mu)\Phi_{IJ}^{(0,2)} + \mu\Phi_{IJ}^{(2,0)} \end{bmatrix}. \quad (4.6)$$

Note that the derivatives of the residual with respect to the nodal temperatures are not included due to the staggered coupling scheme.

Substituting (2.2) and (2.3) in (2.7), the traction condition can be expressed in index notation as

$$\sigma_{ij}n_j - \bar{t}_i = \lambda u_{i,j}n_i + \mu(u_{i,j} + u_{j,i})n_j - 2\alpha'_v(\lambda + \mu)\theta n_i - \bar{t}_i = 0. \quad (4.7)$$

This is expanded as

$$\begin{aligned}
& (\lambda + 2\mu)n_1u_{1,1} + \mu n_2u_{1,2} + \lambda n_1u_{2,2} + \mu n_2u_{2,1} \\
& - 2\alpha'_v(\lambda + \mu)\theta n_1 - \bar{t}_1 = 0 \\
& \lambda n_2u_{1,1} + \mu n_1u_{1,2} + (\lambda + 2\mu)n_2u_{2,2} + \mu n_1u_{2,1} \\
& - 2\alpha'_v(\lambda + \mu)\theta n_2 - \bar{t}_2 = 0.
\end{aligned} \quad (4.8)$$

Then, following the example of the interior nodes, if $\mathbf{x}_I \in \Gamma_t^\alpha$ is a prescribed traction boundary node, the discretized equation at node \mathbf{x}_I is expressed as

$$\begin{aligned}
R_{I1}^{\text{trac}} &:= \sum_{J=1}^N \left[\left((\lambda + 2\mu)n_1\Phi_{IJ}^{(1,0)} + \mu n_2\Phi_{IJ}^{(0,1)} \right) u_1^h(\mathbf{x}_J) \right. \\
&\quad \left. + \left(\lambda n_1\Phi_{IJ}^{(0,1)} + \mu n_2\Phi_{IJ}^{(1,0)} \right) u_2^h(\mathbf{x}_J) \right] \\
&\quad - \sum_{J=1}^N \left(2\alpha'_v(\lambda + \mu)n_1\Phi_{IJ}^{(0,0)} \right) \theta^h(\mathbf{x}_J) - \bar{t}_1(\mathbf{x}_I) \\
R_{I2}^{\text{trac}} &:= \sum_{J=1}^N \left[\left(\lambda n_2\Phi_{IJ}^{(1,0)} + \mu n_1\Phi_{IJ}^{(0,1)} \right) u_1^h(\mathbf{x}_J) \right. \\
&\quad \left. + \left((\lambda + 2\mu)n_2\Phi_{IJ}^{(0,1)} + \mu n_1\Phi_{IJ}^{(1,0)} \right) u_2^h(\mathbf{x}_J) \right] \\
&\quad - \sum_{J=1}^N \left(2\alpha'_v(\lambda + \mu)n_2\Phi_{IJ}^{(0,0)} \right) \theta^h(\mathbf{x}_J) - \bar{t}_2(\mathbf{x}_I).
\end{aligned} \quad (4.9)$$

For convenience in discretizing the contact constraints in Sect. 4.2, the non-constant part of (4.9) will be denoted

$$\mathbf{y}_I^{\text{trac}} := \mathbf{R}_I^{\text{trac}} + \bar{\mathbf{t}}(\mathbf{x}_I). \quad (4.10)$$

Each corresponding IJ block of the tangent stiffness \mathbf{K}_U for $\mathbf{x}_I \in \Gamma_t^\alpha$ is then given by

$$\mathbf{K}_{IJ}^{\text{trac}} = \begin{bmatrix} (\lambda + 2\mu)n_1\Phi_{IJ}^{(1,0)} + \mu n_2\Phi_{IJ}^{(0,1)} & \lambda n_1\Phi_{IJ}^{(0,1)} + \mu n_2\Phi_{IJ}^{(1,0)} \\ \lambda n_2\Phi_{IJ}^{(1,0)} + \mu n_1\Phi_{IJ}^{(0,1)} & (\lambda + 2\mu)n_2\Phi_{IJ}^{(0,1)} + \mu n_1\Phi_{IJ}^{(1,0)} \end{bmatrix}. \quad (4.11)$$

Finally, if $\mathbf{x}_I \in \Gamma_u^\alpha$ is a prescribed displacement boundary node, the discretized equation at node \mathbf{x}_I is simply expressed as

$$\begin{aligned}
R_{I1}^{\text{disp}} &:= \sum_{J=1}^N \Phi_{IJ}^{(0,0)} u_1^h(\mathbf{x}_J) - \bar{u}_1 \\
R_{I2}^{\text{disp}} &:= \sum_{J=1}^N \Phi_{IJ}^{(0,0)} u_2^h(\mathbf{x}_J) - \bar{u}_2.
\end{aligned} \quad (4.12)$$

Each corresponding IJ block of the tangent stiffness \mathbf{K}_U for $\mathbf{x}_I \in \Gamma_u^\alpha$ is then given by

$$\mathbf{K}_{IJ}^{\text{disp}} = \begin{bmatrix} \Phi_{IJ}^{(0,0)} & 0 \\ 0 & \Phi_{IJ}^{(0,0)} \end{bmatrix}. \quad (4.13)$$

In the event that there is a mixed boundary condition at a node, e.g., a roller boundary condition, the appropriate discretized equations can be formulated as a suitable hybrid of (4.9) and (4.12). Given these discretized boundary conditions and governing PDE for the interior nodes (4.5), the full tangent stiffness matrix and residual vector are almost ready to be assembled. Notice that the equations developed so far are linear due to the linear elastic constitutive law and small

displacement and strain assumption. The nonlinearity for the contact problem in this study comes solely from the contact constraints, discretized in the following section.

4.2 Discretization of regularized mechanical contact constraints

Like the traction boundary condition (2.7)₂, the contact condition (2.7)₃ contains the $\sigma \mathbf{n}$ term. Unlike prescribed traction $\bar{\mathbf{t}}$, however, the contact traction \mathbf{t}^c depends on the displacement field. To discretize the contact constraints, we begin by substituting (2.10) in (2.7)₃ and writing this equation in index notation:

$$\sigma_{ij} n_j - t_i^c = \lambda u_{j,j} n_i + \mu (u_{i,j} + u_{j,i}) n_j - t_N v_i + t_T \tau_i = 0. \quad (4.14)$$

The values of contact pressure t_N and tangential traction t_T depend on the gap function and the slip/stick state of the system, as explained in Sect. 2. The gap function is discretized in terms of both the primary contact node $\mathbf{x}_I^\alpha \in \Gamma_c^\alpha$ and the corresponding contact node $\mathbf{x}_I^\beta \in \Gamma_c^\beta$ as follows:

$$g(\mathbf{x}_I^\alpha) \approx G_I := g_0(\mathbf{x}_I^\alpha) - \sum_{j=1}^N \left(\Phi_{IJ}^{(0,0)} - \Phi_{I'J}^{(0,0)} \right) \left[v_1 u_1^h(\mathbf{x}_J) + v_2 u_2^h(\mathbf{x}_J) \right]. \quad (4.15)$$

Here, $\Phi_{IJ}^{(0,0)}$ is the reinterpolation operator for \mathbf{x}_I^α , while $\Phi_{I'J}^{(0,0)}$ is the reinterpolation operator for \mathbf{x}_I^β . The initial gap g_0 is known a priori based on the undeformed geometry of the problem. Similarly, the relative tangential displacement is discretized as follows:

$$\psi(\mathbf{x}_I^\alpha) \approx \Psi_I := \sum_{j=1}^N \left(\Phi_{IJ}^{(0,0)} - \Phi_{I'J}^{(0,0)} \right) \left[\tau_1 u_1^h(\mathbf{x}_J) + \tau_2 u_2^h(\mathbf{x}_J) \right]. \quad (4.16)$$

In the event that the bodies are not in contact (i.e., $g < 0$) at two corresponding contact points, there is neither contact pressure nor tangential traction between the bodies at those points. Thus, for a node $\mathbf{x}_I \in \Gamma_c^\alpha$ for which $g < 0$,

$$\begin{aligned} R_{I1}^{g<0} &:= y_{I1}^{\text{trac}} \\ R_{I2}^{g<0} &:= y_{I2}^{\text{trac}}. \end{aligned} \quad (4.17)$$

Here, y_I^{trac} is given by (4.10). Each corresponding IJ block of \mathbf{K}_U is given by

$$\mathbf{K}_{IJ}^{g<0} = \mathbf{K}_{IJ}^{\text{trac}}. \quad (4.18)$$

Notice that this case is equivalent to a traction-free boundary condition.

If the gap between two corresponding contact points $\mathbf{x}_I^\alpha \in \Gamma_c^\alpha$ and $\mathbf{x}_I^\beta \in \Gamma_c^\beta$ is closed and the points are under the

stick condition, then substituting (2.16) and (2.18) in (4.14), expanding, and applying the differential operators yields

$$\begin{aligned} R_{I1}^{\text{stick}} &:= y_{I1}^{\text{trac}} - \epsilon_N G_I v_1 + \epsilon_T \Psi_I \tau_1 \\ R_{I2}^{\text{stick}} &:= y_{I2}^{\text{trac}} - \epsilon_N G_I v_2 + \epsilon_T \Psi_I \tau_2 \end{aligned} \quad (4.19)$$

Note that the terms involving the gap function have been discretized using (4.15). Differentiating the normal and tangential traction terms with respect to u_1^h and u_2^h leads to the expression for the IJ blocks of \mathbf{K}_U for each $\mathbf{x}_I^\alpha \in \Gamma_c^\alpha$, $\alpha \in \{1, 2\}$:

$$\begin{aligned} \mathbf{K}_{IJ}^{\text{stick}} &= \mathbf{K}_{IJ}^{\text{trac}} - \epsilon_N \left(\Phi_{IJ}^{(0,0)} - \Phi_{I'J}^{(0,0)} \right) \begin{bmatrix} v_1 v_1 & v_1 v_2 \\ v_2 v_1 & v_2 v_2 \end{bmatrix} \\ &\quad + \epsilon_T \left(\Phi_{IJ}^{(0,0)} - \Phi_{I'J}^{(0,0)} \right) \begin{bmatrix} \tau_1 \tau_1 & \tau_1 \tau_2 \\ \tau_2 \tau_1 & \tau_2 \tau_2 \end{bmatrix} \end{aligned} \quad (4.20)$$

Finally, if the gap between \mathbf{x}_I^α and \mathbf{x}_I^β is closed and the two points are under the slip condition, then substituting (2.16) and (2.20) in (4.14), expanding, and applying the differential operators yields

$$\begin{aligned} R_{I1}^{\text{slip}} &:= y_{I1}^{\text{trac}} - \epsilon_N G_I v_1 + \mu_f \epsilon_N G_I \text{sign}(\Psi_I) \tau_1 \\ R_{I2}^{\text{slip}} &:= y_{I2}^{\text{trac}} - \epsilon_N G_I v_2 + \mu_f \epsilon_N G_I \text{sign}(\Psi_I) \tau_2. \end{aligned} \quad (4.21)$$

Each corresponding block IJ of \mathbf{K}_U in the case of stick is then given by

$$\begin{aligned} \mathbf{K}_{IJ}^{\text{slip}} &= \mathbf{K}_{IJ}^{\text{trac}} - \epsilon_N \left(\Phi_{IJ}^{(0,0)} - \Phi_{I'J}^{(0,0)} \right) \begin{bmatrix} v_1 v_1 & v_1 v_2 \\ v_2 v_1 & v_2 v_2 \end{bmatrix} \\ &\quad + \mu_f \epsilon_N \text{sign}(\Psi_I) \left(\Phi_{IJ}^{(0,0)} - \Phi_{I'J}^{(0,0)} \right) \begin{bmatrix} \tau_1 v_1 & \tau_1 v_2 \\ \tau_2 v_1 & \tau_2 v_2 \end{bmatrix}. \end{aligned} \quad (4.22)$$

In summary, each portion of the residual vector and block of the tangent stiffness matrix corresponding to a contact collocation point $\mathbf{x}_I^\alpha \in \Gamma_c^\alpha$, $\alpha \in \{1, 2\}$ is given by

$$\mathbf{R}_I^{\text{contU}} = \begin{cases} \mathbf{R}_I^{g<0}, & \text{if } g < 0 \\ \mathbf{R}_I^{\text{stick}}, & \text{if stick} \\ \mathbf{R}_I^{\text{slip}}, & \text{if slip} \end{cases}. \quad (4.23)$$

Each IJ block of the contact condition part of \mathbf{K}_U is given by

$$\mathbf{K}_{IJ}^{\text{contU}} = \begin{cases} \mathbf{K}_{IJ}^{g<0}, & \text{if } g < 0 \\ \mathbf{K}_{IJ}^{\text{stick}}, & \text{if stick} \\ \mathbf{K}_{IJ}^{\text{slip}}, & \text{if slip} \end{cases}. \quad (4.24)$$

These expressions (4.23) and (4.24) may be used in conjunction with the discretized equations in Sect. 4.1 to assemble the total residual vector and tangent stiffness matrix for the problem. No special method of assembly is required, unlike in the context of finite elements; the expressions developed

above are simply concatenated $I = 1 : N$ according to the type (interior, boundary, contact, etc.) of node I . Thus, the I^{th} block of \mathbf{R}_U , i.e., entries $2I - 1$ and $2I$ of \mathbf{R}_U , is given by

$$(\mathbf{R}_U)_I = \begin{cases} \mathbf{R}_I^{\text{intU}}, & \text{if } \mathbf{x}_I \in \Omega \\ \mathbf{R}_I^{\text{trac}}, & \text{if } \mathbf{x}_I \in \Gamma_t \\ \mathbf{R}_I^{\text{disp}}, & \text{if } \mathbf{x}_I \in \Gamma_u \\ \mathbf{R}_I^{\text{contU}}, & \text{if } \mathbf{x}_I \in \Gamma_c \end{cases}. \quad (4.25)$$

Similarly, the IJ block of \mathbf{K}_U is given by

$$(\mathbf{K}_U)_{IJ} = \begin{cases} \mathbf{K}_{IJ}^{\text{intU}}, & \text{if } \mathbf{x}_I \in \Omega \\ \mathbf{K}_{IJ}^{\text{trac}}, & \text{if } \mathbf{x}_I \in \Gamma_t \\ \mathbf{K}_{IJ}^{\text{disp}}, & \text{if } \mathbf{x}_I \in \Gamma_u \\ \mathbf{K}_{IJ}^{\text{contU}}, & \text{if } \mathbf{x}_I \in \Gamma_c \end{cases}. \quad (4.26)$$

Note that the tangent stiffness matrix \mathbf{K}_U is discontinuous at the transitions between non-contact and contact, and between stick and slip. For this reason, the Newton–Raphson iteration using \mathbf{R}_U and \mathbf{K}_U is not guaranteed to converge mathematically. However, in practice, this process does converge for the problems considered in this study, so smoother regularizations of the contact pressure and tangential traction are not considered. It would be straightforward to modify these expressions to have continuous first and second derivatives using, for example, Hermite interpolation of contact pressure and tangential traction in a user-defined radius around $g = 0$, $\psi = 0$, and $\Phi^{\text{trial}} = 0$.

4.3 Discretization of thermal equations

The thermal governing equation, boundary conditions, and contact constraints are discretized in a similar fashion. When (2.6) is substituted in (2.5) and expanded, the result is Poisson's equation:

$$-\kappa(\theta_{,11} + \theta_{,22}) + s = 0. \quad (4.27)$$

Thus, for an interior collocation point $\mathbf{x}_I \in \Omega$, this is discretized as

$$R_I^{\text{intT}} := \sum_{J=1}^N \left[-\kappa \left(\Phi_{IJ}^{(2,0)} + \Phi_{IJ}^{(0,2)} \right) \theta^h(\mathbf{x}_J) \right] + s(\mathbf{x}_I). \quad (4.28)$$

The IJ entry of \mathbf{K}_T corresponding to $\mathbf{x}_I \in \Omega$ is then given by

$$K_{IJ}^{\text{intT}} = -\kappa \left(\Phi_{IJ}^{(2,0)} + \Phi_{IJ}^{(0,2)} \right). \quad (4.29)$$

The prescribed heat flux boundary condition is expanded to yield

$$-\kappa(\theta_{,1}n_1 + \theta_{,2}n_2) - \bar{q} = 0. \quad (4.30)$$

Thus, for a prescribed heat flux boundary point $\mathbf{x}_I \in \Gamma_q$, this is discretized as

$$R_I^{\text{flux}} := \sum_{J=1}^N \left[-\kappa \left(\Phi_{IJ}^{(1,0)}n_1 + \Phi_{IJ}^{(0,1)}n_2 \right) \theta^h(\mathbf{x}_J) \right] - \bar{q}(\mathbf{x}_I). \quad (4.31)$$

For convenience in discretizing the contact condition, let $y_I^{\text{flux}} = R_I^{\text{flux}} + \bar{q}(\mathbf{x}_I)$. The IJ entry of \mathbf{K}_T corresponding to $\mathbf{x}_I \in \Gamma_q$ is then given by

$$K_{IJ}^{\text{flux}} = -\kappa \left(\Phi_{IJ}^{(1,0)}n_1 + \Phi_{IJ}^{(0,1)}n_2 \right). \quad (4.32)$$

The discretized equation for a prescribed temperature boundary collocation point $\mathbf{x}_I \in \Gamma_\theta$ is simply given by

$$R_I^{\text{temp}} := \sum_{J=1}^N \left[\Phi_{IJ}^{(0,0)} \theta^h(\mathbf{x}_J) \right] - \bar{\theta}(\mathbf{x}_I). \quad (4.33)$$

The IJ entry of \mathbf{K}_T corresponding to $\mathbf{x}_I \in \Gamma_\theta$ is then given by

$$K_{IJ}^{\text{temp}} = \Phi_{IJ}^{(0,0)}. \quad (4.34)$$

Finally, if $\mathbf{x}_I^\alpha \in \Gamma_c^\alpha$ is a contact node and $\mathbf{x}_I^\beta \in \Gamma_c^\beta$ is its corresponding contact node on the other body, the discretized form of the thermal contact condition is given by

$$R_I^{\text{contT}} := y_I^{\text{flux}} - \sum_{J=1}^N \left[h_0 \left(\frac{\epsilon_N \langle G_I \rangle}{H_e} \right)^P \left(\Phi_{IJ}^{(0,0)} - \Phi_{I'J}^{(0,0)} \right) \theta^h(\mathbf{x}_J) \right]. \quad (4.35)$$

Here, as in the discretized mechanical contact constraints, G_I is the discretized gap function (4.15) and $\Phi_{IJ}^{(0,0)}$ and $\Phi_{I'J}^{(0,0)}$ are the reinterpolation operators for \mathbf{x}_I^α and \mathbf{x}_I^β , respectively. Again recalling that the derivative terms with respect to the nodal displacement solution vector are neglected because this study is considering a staggered Newton–Raphson scheme, the IJ entry of the tangent stiffness \mathbf{K}_T is given by

$$K_{IJ}^{\text{contT}} := K_{IJ}^{\text{flux}} - h_0 \left(\frac{\epsilon_N \langle G_I \rangle}{H_e} \right)^P \left(\Phi_{IJ}^{(0,0)} - \Phi_{I'J}^{(0,0)} \right). \quad (4.36)$$

The full residual vector \mathbf{R}_T and tangent stiffness matrix \mathbf{K}_T are assembled in similar fashion as (4.25) and (4.26).

5 Numerical study

In this section, the proposed nonlinear strong-form collocation method is verified through two numerical examples related to two-body mechanical contact alone and one related to thermomechanical contact. The first, involving frictional contact between two blocks along an inclined surface, is used to assess the ability of the proposed method to distinguish

between slip and stick conditions. The second, involving Hertzian contact between two half-cylinders, verifies the method against a nontrivial analytical solution. The third, involving thermomechanical contact between two rectangular blocks, verifies the pressure-dependent thermal contact model and that the mechanical and thermal problems may be accurately solved together using the staggered Newton–Raphson scheme.

5.1 Mechanical contact along an inclined surface

The first numerical example considered in this study concerns mechanical contact between two blocks along an inclined surface. A version of this example was used in [10] to verify a mortared finite-element method for multibody frictional contact. The geometry for this problem is shown in Fig. 3. In their reference configuration, the two blocks together form a square of side length 2.0. They are separated by a contact surface of frictional coefficient μ_f along a line of slope $m = 0.2$ through the centroid of the square. The block below the contact surface is pinned at the bottom right corner and resting on rollers along the remainder of its bottom surface. The top block has a prescribed displacement of $u_y = -0.01$ at its top surface. It is restrained in the x -direction at the top right corner but free in the x -direction along the rest of the top surface. The left and right sides of the block are traction-free. For both blocks, the Young's modulus and Poisson's ratio are $E = 1.0$ and $\nu = 0.3$. The normal and tangential penalty parameters are chosen to be $\epsilon_N = \epsilon_T = 1.0 \times 10^6 E$ (as for the rest of the numerical examples in this section unless otherwise stated).

The purpose of this numerical example is to determine with what sensitivity the proposed method can distinguish between the slip and stick conditions. Theoretically, if the

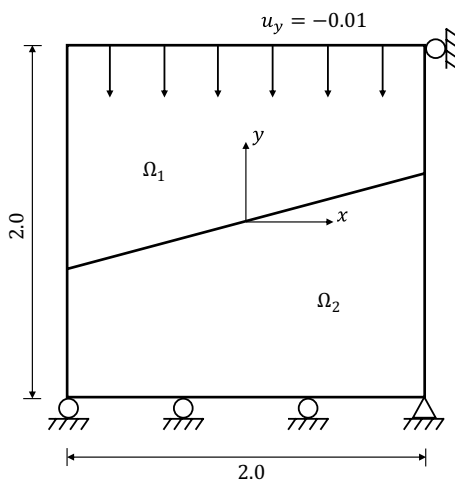


Fig. 3 Free-body diagram for the problem of mechanical contact along an inclined surface

coefficient of friction μ_f is chosen to be greater than the slope of the interface m , then the entire contact surface will be under the stick condition. Conversely, if μ_f is chosen to be less than the slope of the contact interface, then the entire contact surface will be under the slip condition. However, in practice, there will be some threshold coefficient of friction $\mu_{\text{thresh}} \neq m$ above which the contact surface sticks and below which it slips. Thus, how small a difference exists between μ_{thresh} and m is a measure of the sensitivity with which the method can distinguish between stick and slip.

Figure 4 shows an example arrangement of collocation points used for this problem. This arrangement is a uniform Cartesian-product grid perturbed so that the number of contact points along the inclined surface is equal to the number of points along the bottom edge of the domain. Using the nodal arrangement shown in Fig. 4, the displacement field is computed using the proposed method for various values of the friction coefficient μ_f near 0.2. The results of these trials indicate that the threshold friction coefficient for the proposed method is $\mu_{\text{thresh}} = 0.1999997 = m - (3 \times 10^{-7})$. Contour plots of the displacement field are shown for $\mu_f = 0.19$ in Fig. 5 and for $\mu_f = 0.21$ in Fig. 6. Slip is clearly visible in the discontinuity in the u_1 field for $\mu_f = 0.19$ in Fig. 5.

To verify the results of the proposed method for the inclined contact surface example, the contact pressure and tangential traction computed from the method are compared with results from FEM. In addition to the sum of normal contact tractions from each side of the interface (which should be zero in equilibrium), Figs. 7 and 8 show the contact pressure profile along the contact surface according to

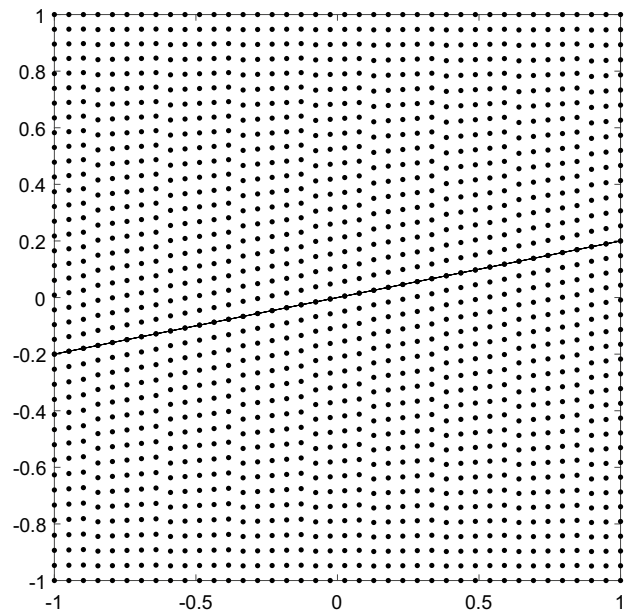


Fig. 4 Example arrangement of collocation points for the inclined surface problem

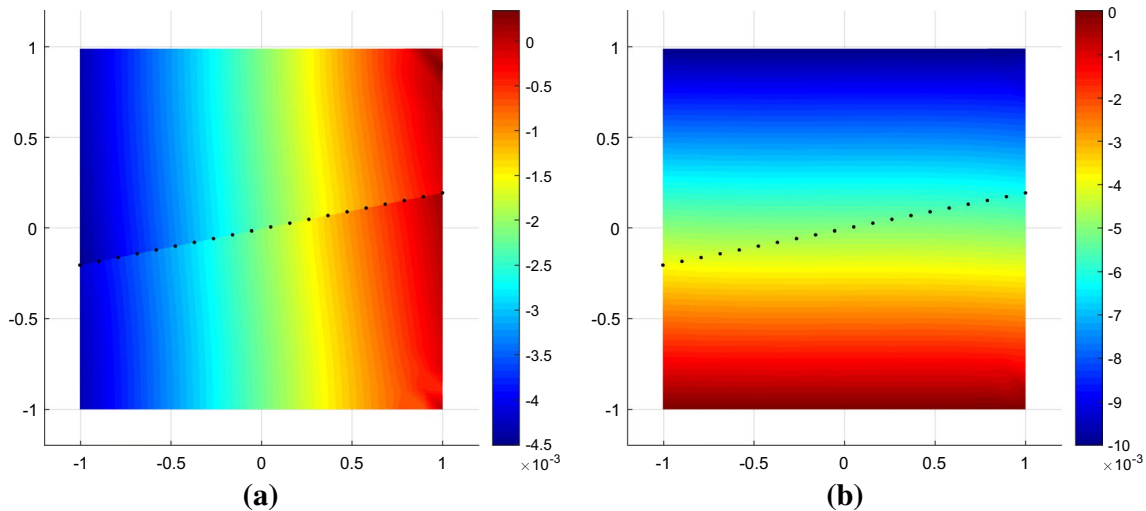


Fig. 5 **a** x-component and **b** y-component of displacement for the inclined surface problem, $\mu_f = 0.19$

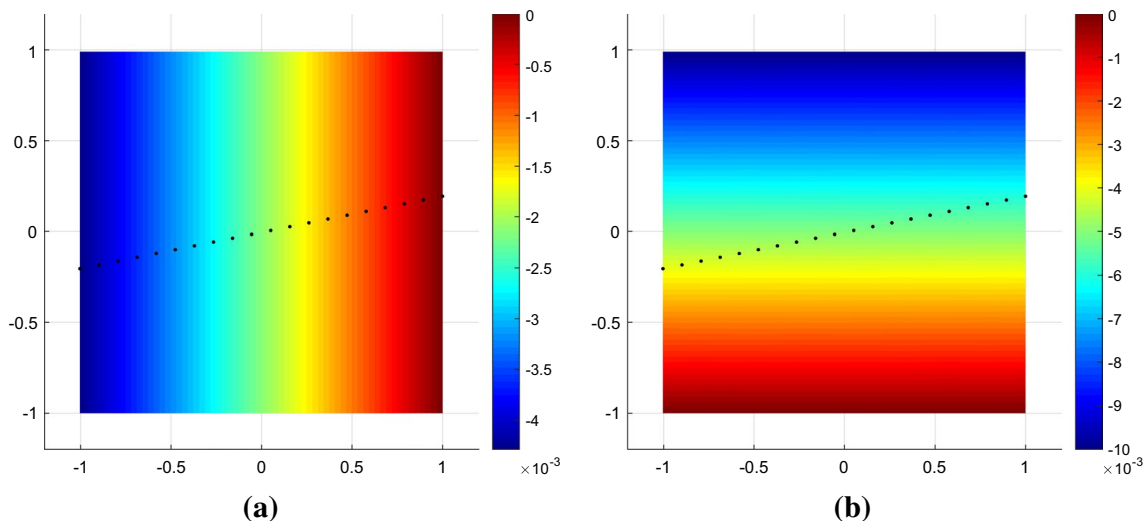


Fig. 6 **a** x-component and **b** y-component of displacement for the inclined surface problem, $\mu_f = 0.21$

the stress field, the contact algorithm, and an ABAQUS FEM model. The FEM model was chosen to have roughly the same level of discretization as the collocation point arrangement in Fig. 4.

A similar comparison is shown in Figs. 9 and 10. For both contact pressure and tangential traction, the results from different parts of the proposed method algorithm agree with each other and with the FEM model.

5.2 Hertzian contact between two half-cylinders

The second numerical example considered in this study concerns Hertzian contact between two half-cylinders. A version of this example was used in [8] for verification purposes. The geometry for this problem is shown in Fig. 11.

As shown, two half-cylinders of radius $R = 8$ are in contact at the origin. They are separated by a flat contact surface of frictional coefficient $\mu_f = 0.2$. The bottom edge of the bottom half-cylinder is fixed in both directions. The top block has a prescribed displacement of $\bar{\mathbf{u}}(x) = \{\bar{u}_x(x), \bar{u}_y(x)\}$ along its top surface. All other boundaries (other than the contact interface) are traction-free. For both bodies, the Young's modulus and Poisson's ratio are $E = 200$ and $\nu = 0.3$. The normal and tangential penalty parameters are again chosen to be $\epsilon_N = \epsilon_T = 1.0 \times 10^4 E$.

The arrangement of collocation points used for this problem is shown in Fig. 12. It is a random arrangement of points generated using the open-source meshing software `gmsh` [43]. The spacing of collocation points around the contact point is much smaller than that in the rest of the domain to

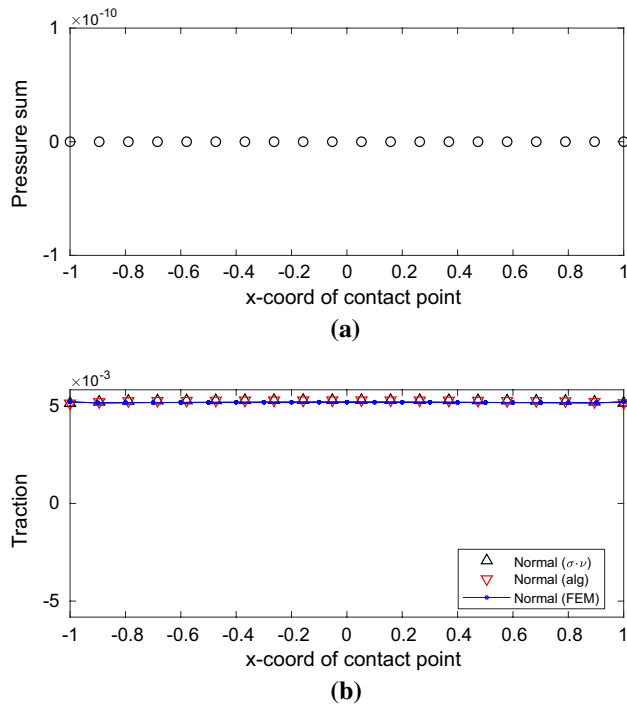


Fig. 7 **a** Sum of normal tractions from top and bottom surface of contact interface and **b** contact pressure from stress, contact algorithm, and FEM for $\mu_f = 0.19$

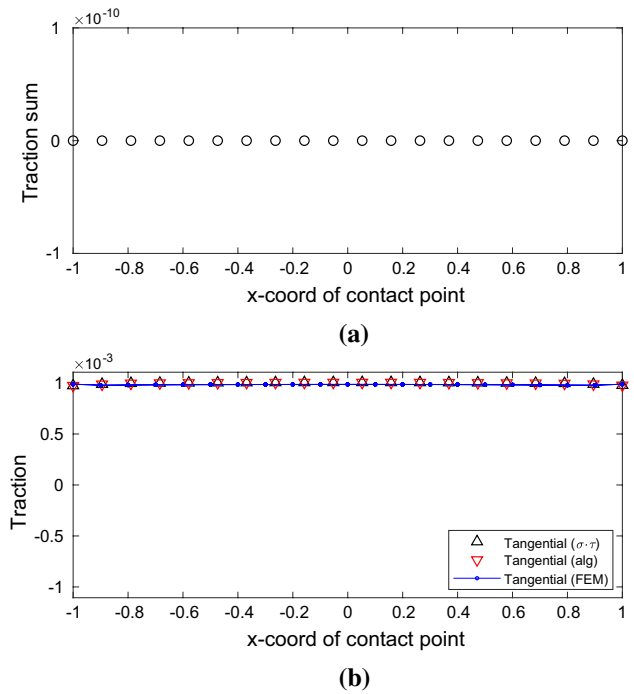


Fig. 9 **a** Sum of tangential tractions from top and bottom surface of contact interface and **b** tangential traction from stress, contact algorithm, and FEM for $\mu_f = 0.19$

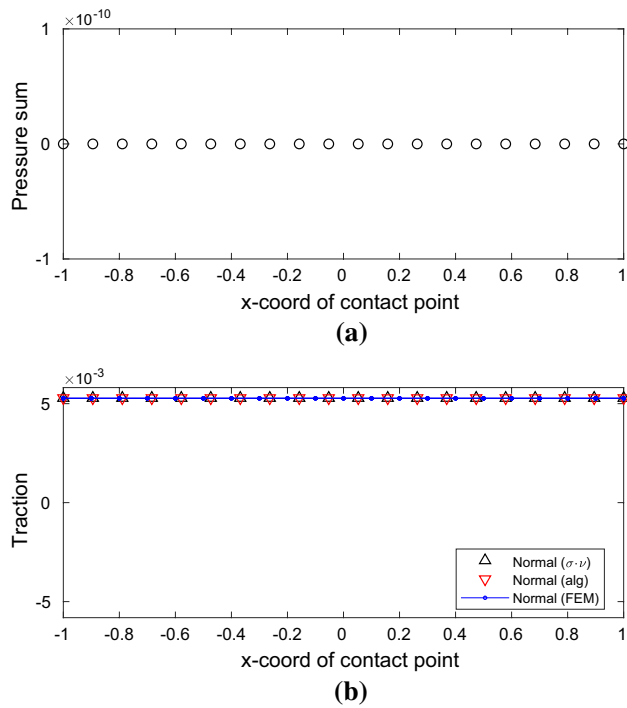


Fig. 8 **a** Sum of normal tractions from top and bottom surface of contact interface and **b** contact pressure from stress, contact algorithm, and FEM for $\mu_f = 0.21$

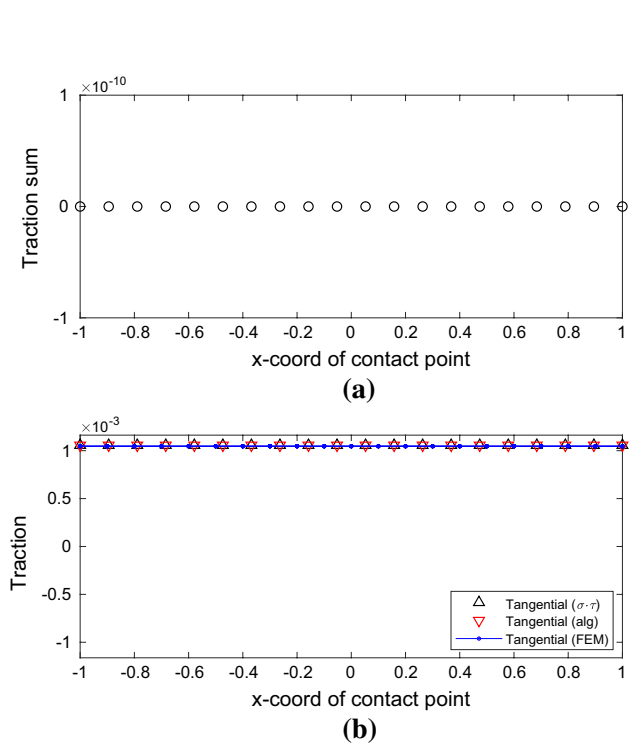


Fig. 10 **a** Sum of tangential tractions from top and bottom surface of contact interface and **b** tangential traction from stress, contact algorithm, and FEM for $\mu_f = 0.21$

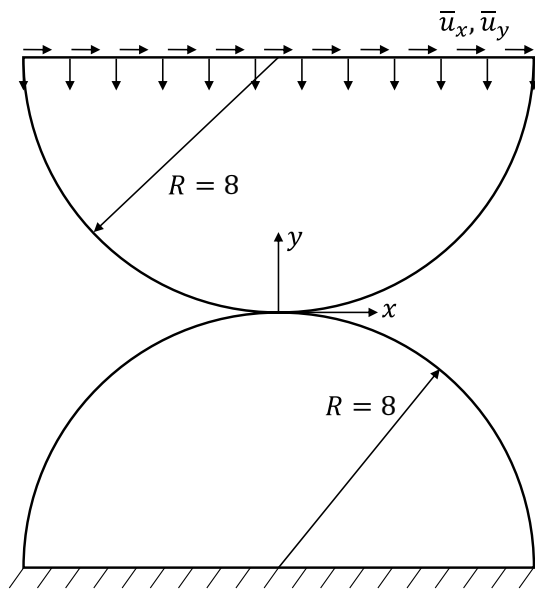


Fig. 11 Free-body diagram for Hertzian contact problem

ensure a sufficient number of contact nodes and local precision of the solution.

Before applying both horizontal and vertical loads to the top edge of the top cylinder, a simplified case is considered in which $\mu_f = 0$ and only vertical loading is applied. Under these conditions, $x = 0$ is a line of symmetry, allowing half the problem to be considered. When only half the problem is considered, the numerical algorithm proposed here is sufficiently stable that a vertical traction may be considered at

the top surface (When the full problem is considered, the algorithm becomes unstable because the top cylinder is not sufficiently constrained and undergoes uncontrolled rigid body motion). For the Hertzian contact problem with only vertical traction loading, an analytical solution is available. Thus, we can use this example to compare the results from the proposed method with an analytical solution for a problem in which the contact traction distribution is nontrivial. The analytical solution for contact pressure along the contact surface was provided by Ref. [44] and is given by the elliptical profile

$$t_N(x) = \frac{2p_{\text{top}}}{\pi a^2} (a^2 - x^2)^{1/2}. \quad (5.1)$$

Here, p_{top} is the prescribed normal traction at the top edge. The value of a is found from

$$a = \sqrt{\frac{4p_{\text{top}}R}{\pi E}}. \quad (5.2)$$

In (5.2), R is the radius of the cylinder and E is the Young's modulus of the cylinders. Contour plots of the x - and y -components of displacement computed using the proposed method are given in Fig. 13. A comparison between the contact pressure computed from the proposed method and that from the exact solution is shown in Fig. 14. Figure 14 shows agreement between the proposed method and the exact solution, particularly with respect to the peak contact pressure. There is higher error in the contact pressure

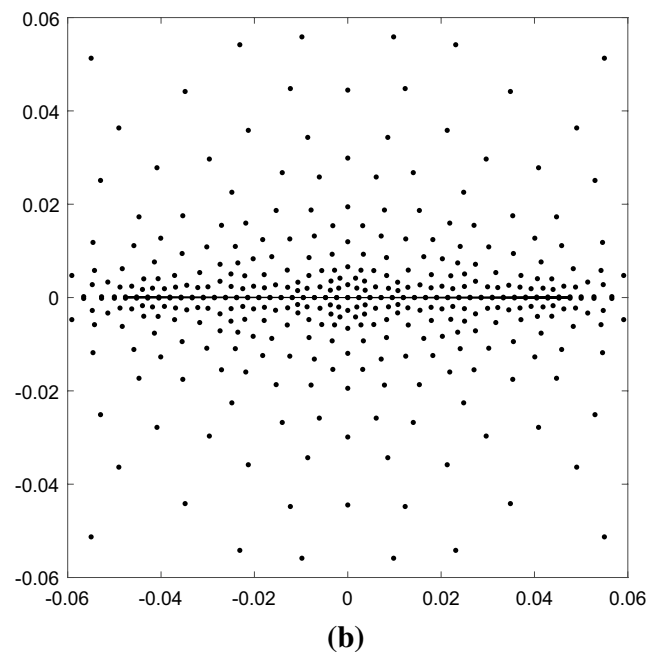
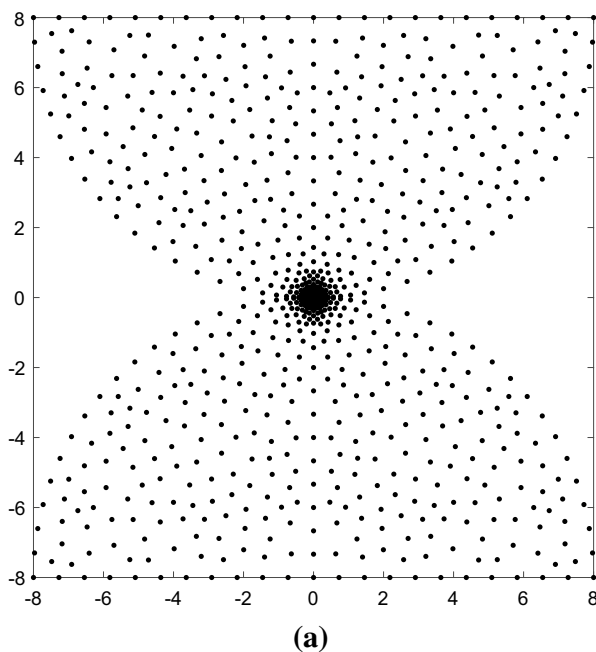


Fig. 12 **a** Arrangement of collocation points for the Hertzian contact problem and **b** detail of nodal arrangement near contact surface

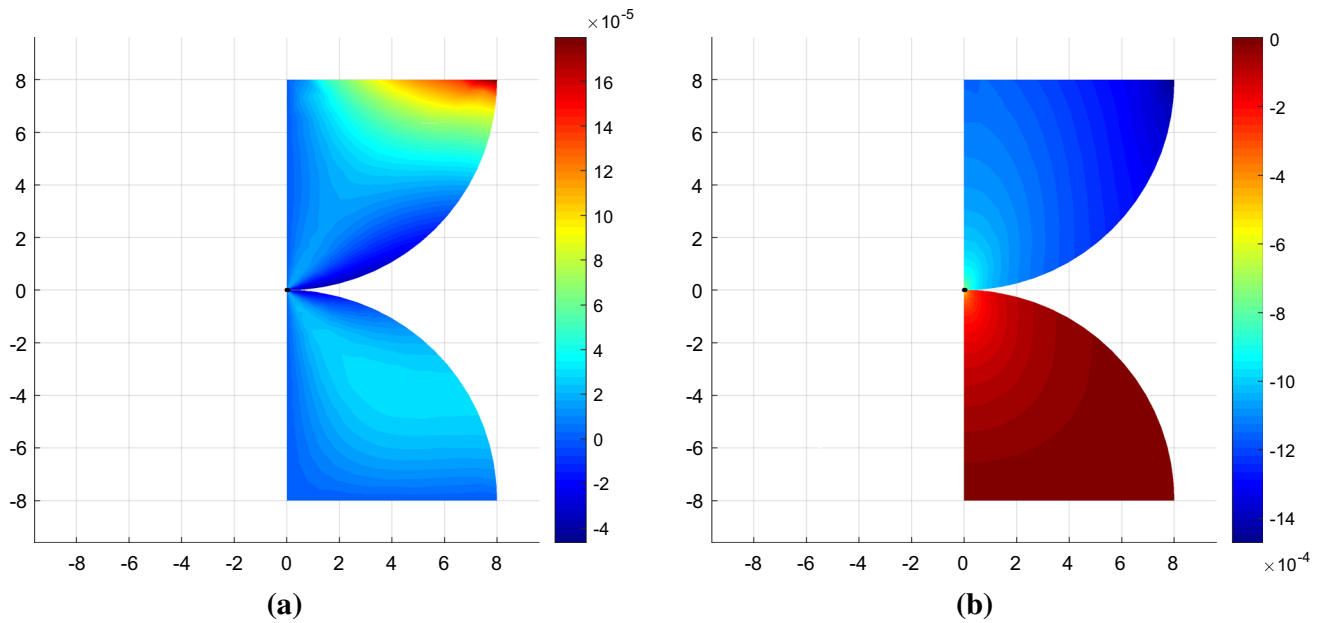


Fig. 13 **a** x -component and **b** y -component of displacement for the half-Hertzian contact problem according to the proposed method

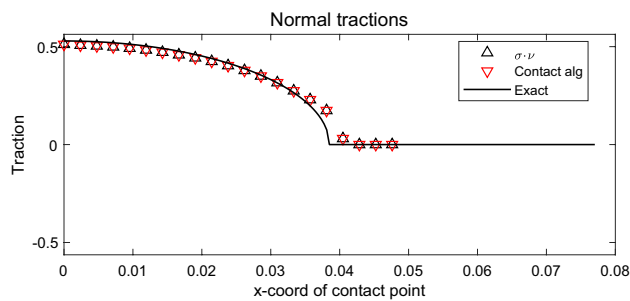


Fig. 14 Contact pressure profile for half-Hertzian contact problem

near the edge of the contact boundary. However, as the collocation point arrangement is further refined, the discrepancy between the computed and analytical solution near the edge of the contact boundary is reduced. It should also be noted that finite-element methods such as [9] experience similar difficulties.

Next, the full Hertzian contact problem is solved using the proposed method. The numerical solution to the full problem with $\bar{\mathbf{u}} = \{0.0002, -0.0014\}$ is shown in Fig. 15.

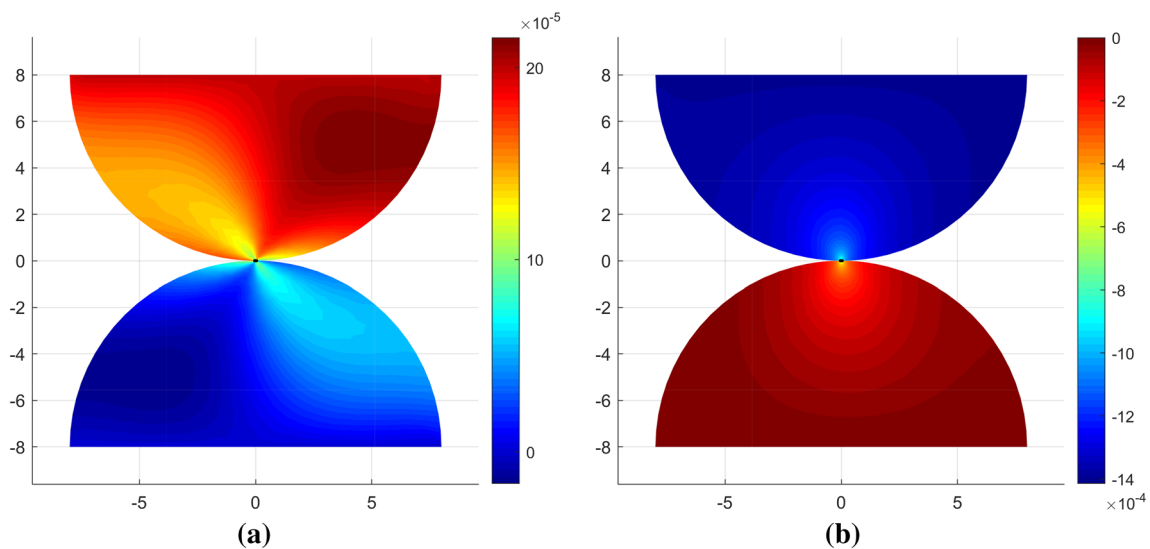


Fig. 15 **a** x -component and **b** y -component of displacement for the full Hertzian contact problem according to the proposed method

5.3 Thermomechanical contact between rectangular blocks

In this section, thermomechanical contact between rectangular blocks is examined. A version of this example was used in [4] to verify an enriched finite-element method for thermomechanical contact. The geometry and uniform nodal arrangement for this problem are shown in Fig. 16. Each block is a square of side length 1.0 m. They are separated by a contact surface of frictional coefficient $\mu_f = 0.2$, resistivity coefficient $h_0 = 1.0$, resistivity exponent $P = 1.5$, and Vickers hardness $H_e = 3.0$ along a horizontal line through the origin. The block below the contact surface is fixed in both directions along its bottom surface and is fixed at a temperature change of 0 K. The top block has a prescribed displacement of $\mathbf{u} = \{0, \bar{u}_y\}$ and prescribed temperature of 100 K along its top surface. The left and right sides of the blocks are traction-free and perfectly insulated. For both blocks, the Young's modulus and Poisson's ratio are $E = 0.07 \text{ MPa}$ and $\nu = 0.3$, while the thermal conductivity and expansion coefficient are

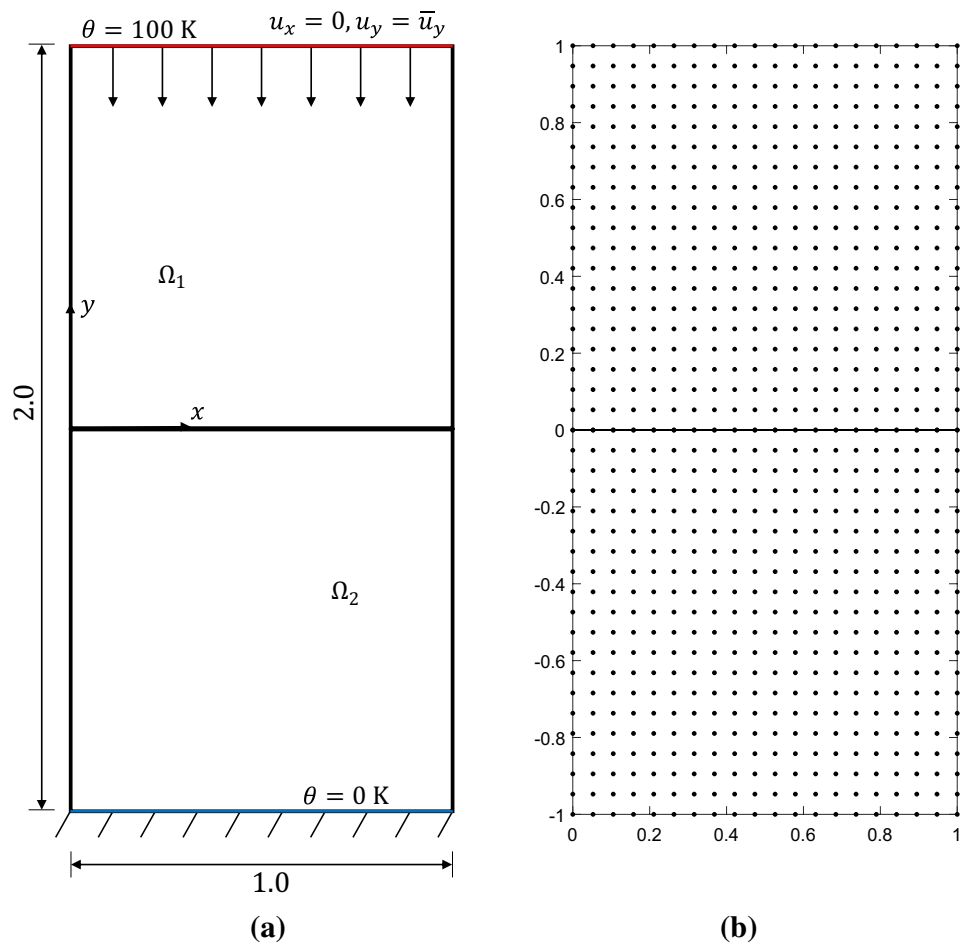
$\kappa = 150 \text{ J/m} \cdot \text{s} \cdot \text{K}$ and $\alpha_v = 1.0 \times 10^{-7} \text{ K}^{-1}$. The normal and tangential penalty parameters are $\epsilon_N = \epsilon_T = 1.0 \times 10^4 E$.

Using this numerical example, the implementation of the pressure-dependent thermal contact model can be verified using an analytical solution for the temperature on either side of the contact interface. Specifically, for the pressure-dependent model, the contact boundary temperatures are given in [4] and originally in [6] by

$$\begin{aligned}\theta^+ &= \frac{(\kappa + h(t_N))\theta_{\text{top}} + h(t_N)\theta_{\text{bottom}}}{\kappa + 2h(t_N)} \\ \theta^- &= \frac{(\kappa + h(t_N))\theta_{\text{bottom}} + h(t_N)\theta_{\text{top}}}{\kappa + 2h(t_N)}.\end{aligned}\quad (5.3)$$

Here, θ^+ and θ^- are the temperatures on the edge above and below the contact surface, respectively, θ_{top} and θ_{bottom} are the prescribed temperatures at the top and bottom edges of the entire domain, respectively, and $h(t_N)$ is given by (2.22). To find the temperature profiles along the contact interface numerically, the proposed method is used with the uniform nodal arrangement shown in Fig. 16 to solve the contact

Fig. 16 **a** Free-body diagram and **b** arrangement of collocation points for the problem of thermomechanical contact between rectangular blocks



problem for various values of prescribed displacement. Figure 17 shows contour plots of the components of displacement and temperature for $\bar{u}_y = -1.0 \times 10^{-3}$. The computed displacement and temperature fields in Fig. 17 are reasonable. As expected in the x -displacement field, the top and bottom edges are held fixed in the x -direction while the left and right sides experience a Poisson's effect. The y -component of displacement has an approximately constant slope in the y -direction, as expected since the two blocks have the same material properties. Any discrepancy from constant strain ϵ_{yy} can be explained by the thermal expansion of the top block. Finally, the temperature field has a jump at the contact interface but there is a temperature gradient across each block, reflecting the imperfect, i.e., *flux-resistant* heat conduction across the interface modeled by Eq. (2.22).

Beyond these initial assurances, the numerical solution is verified by its agreement with the analytical solution for the temperature jump across the contact interface. The analytical temperatures along the contact interface are computed based on the computed contact pressure because an analytical solution based directly on prescribed displacement is unavailable. Figure 18 shows that the temperature jump across the contact interface becomes smaller as the contact pressure increases because the increased contact pressure makes the surface more conductive, as expected.

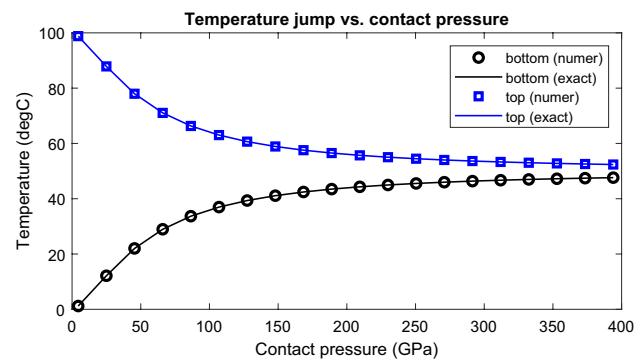


Fig. 18 Temperature jump across contact interface for various values of contact pressure

It also shows that the analytical temperature vs. contact pressure is visually indistinguishable from the computed solution. The maximum relative error between the analytical temperature and the computed temperature is

$$\frac{\max|\theta_{\text{exact}} - \theta_{\text{numer}}|}{\max|\theta_{\text{exact}}|} = 2.3 \times 10^{-4}. \quad (5.4)$$

The numerical results from this section verify the implementation of the proposed method for thermomechanical contact. From the first example, it is clear that the method

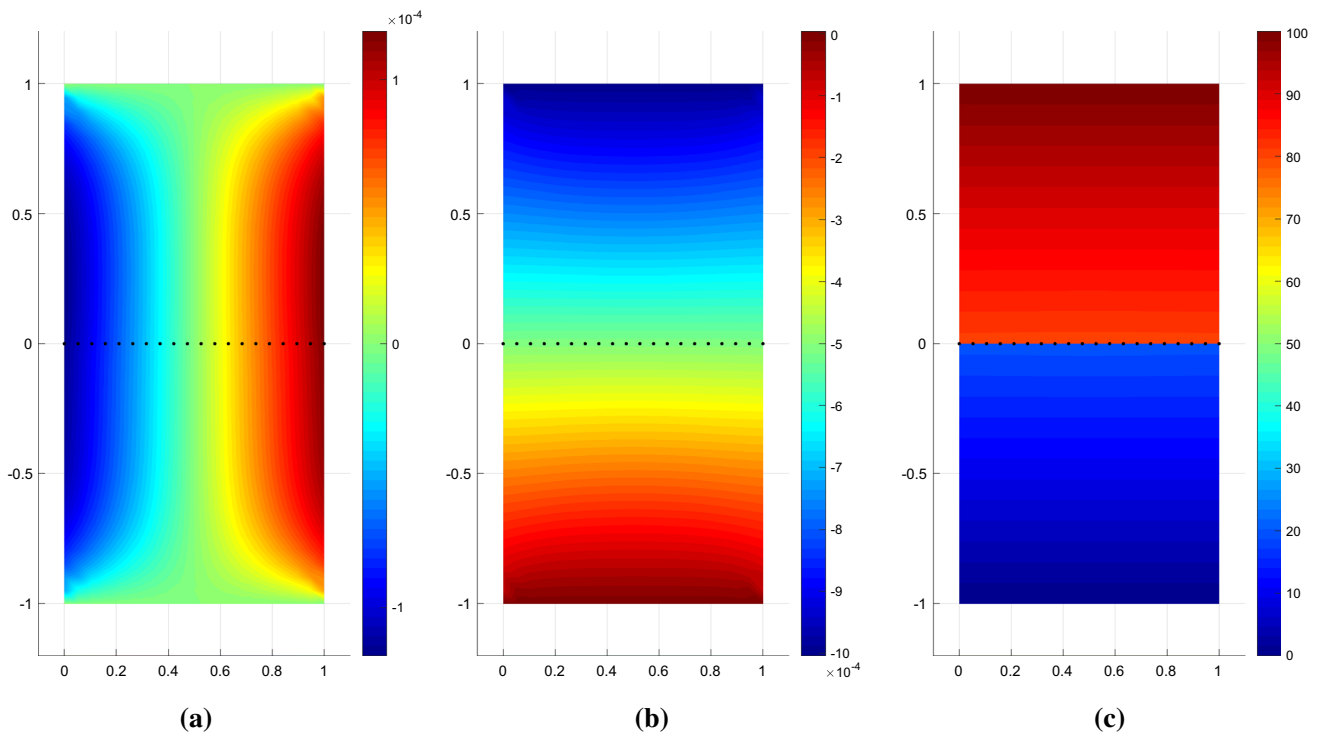


Fig. 17 **a** x -component of displacement, **b** y -component of displacement, and **c** temperature for the problem of thermomechanical contact between rectangular blocks

can accurately distinguish between stick and slip in the case of frictional contact. The second example (Hertzian contact) demonstrates that the proposed method can successfully match the analytical solution for a nontrivial contact pressure profile in the frictionless case and predict a reliable numerical solution of the governing equations in the frictional case. Based on the third example, the method can handle the additional nonlinearity of the thermal field, since the method accurately predicts the temperature jump across the contact interface for various levels of contact pressure. The results from this study are promising for future developments

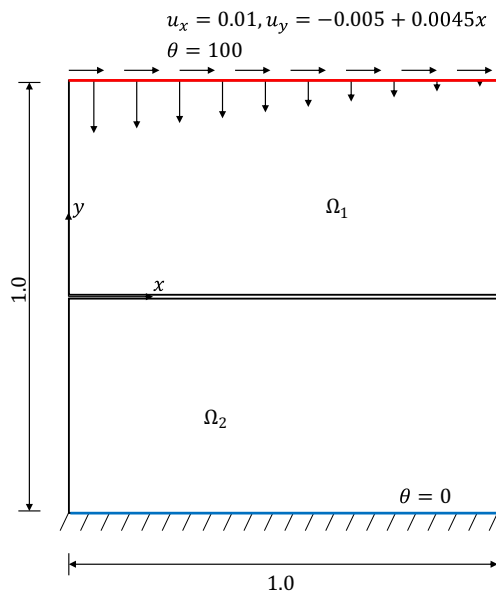


Fig. 19 Free-body diagram for thermomechanical contact between rectangular blocks with nonuniform vertical and nonzero horizontal prescribed displacement along the top surface

to the strong-form meshfree collocation framework for thermomechanical contact.

5.4 Thermomechanical contact between rectangular blocks with sliding

Thermomechanical contact between rectangular blocks is again considered in this section. In contrast to the previous section, however, nonuniform vertical displacement and nonzero horizontal displacement are prescribed at the top of the block. The geometry for this problem is shown in Fig. 19. Together, the blocks form a $1.0 \times 1.0 \text{ m}^2$. They are separated by a contact surface of frictional coefficient $\mu_f = 0.4$, resistivity coefficient $h_0 = 6.5 \times 10^{-5}$, resistivity exponent $P = 1.0$, and Vickers hardness $H_e = 100$ along a horizontal line through the origin. The block below the contact surface is fixed in both directions along its bottom surface and is fixed at a temperature change of 0 K. The top block has a prescribed displacement of $\mathbf{u} = \{0.01, -0.005 + 0.0045x\}$ meters and a prescribed temperature of 100 K along its top surface. The left and right sides of the blocks are traction-free and perfectly insulated. For both blocks, the Young's modulus and Poisson's ratio are $E = 1.0 \times 10^4 \text{ MPa}$ and $\nu = 0.3$, while the thermal conductivity and expansion coefficient are $\kappa = 150 \text{ J/m} \cdot \text{s} \cdot \text{K}$ and $\alpha_v = 1.0 \times 10^{-8} \text{ K}^{-1}$. The normal and tangential penalty parameters are $\epsilon_N = \epsilon_T = 1.0 \times 10^4 E$.

The loading conditions in this example give rise to nonuniform traction and heat flux profiles along the contact surface. Figure 20 shows contour plots of the components of displacement and temperature for this example. The computed displacement and temperature fields in Fig. 20 are reasonable. The nonzero x -displacement prescribed at the top surface leads to slip between the top and bottom blocks, as evidenced by the discontinuity in the x -displacement at the contact surface. Note that the

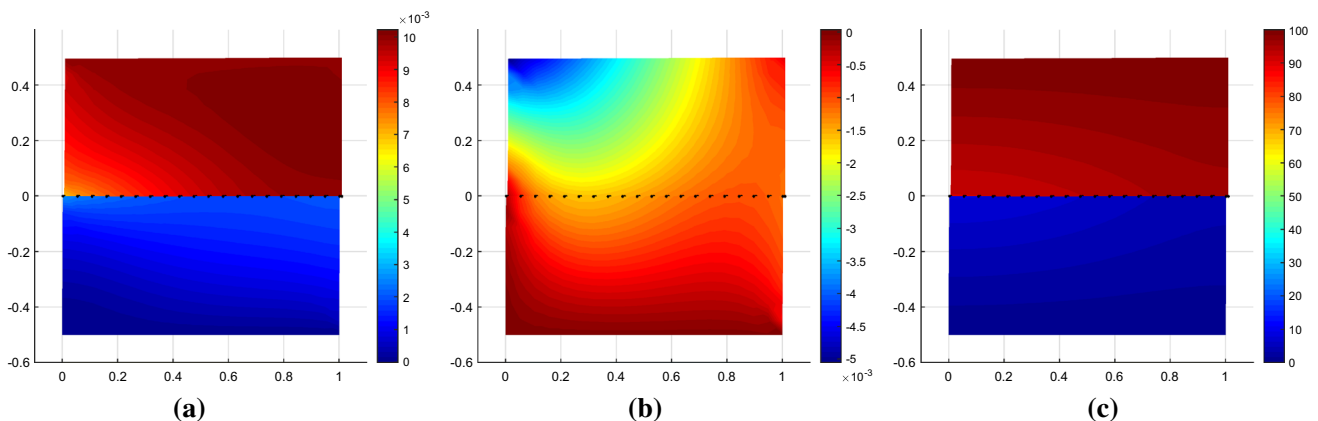


Fig. 20 **a** x -component of displacement, **b** y -component of displacement, and **c** temperature for the problem of thermomechanical contact between rectangular blocks with sliding

larger y -displacement prescribed at the top left edge of the domain than at the top right causes a stress concentration as shown in Fig. 20b.

6 Conclusion

To solve the nonlinear equations of multibody thermomechanical contact, the proposed strong-form meshfree collocation method was adapted to a staggered Newton–Raphson framework. In each verification and numerical example presented, the solution by the proposed method agreed with analytical or finite-element solutions or was physically reasonable. In the inclined interface verification example, the method demonstrated a marked ability to distinguish between the stick and slip conditions and the contact traction profile agreed with results from commercial FEM software. The proposed method solution was shown to agree with the analytical solution for frictionless Hertzian contact, for which the contact pressure profile at the contact interface is nontrivial. Moreover, the method yielded a reasonable numerical solution for the Hertzian contact with friction. Finally, the method was shown to be accurate even with the additional nonlinearity introduced by the thermomechanical coupling, as evidenced by the example involving thermomechanical contact between rectangular blocks. Now that the proposed method has been verified for mechanical and thermomechanical contact, it can be used for more realistic applications, such as modeling of thermomechanical interactions in a nuclear fuel rod.

Future work will further explore the capability of the proposed method for more realistic contact problems. Expanding the capabilities of the contact framework presents numerous challenges, including the additional material and geometric nonlinearities introduced, the need to implement a contact search algorithm and built-in adaptive refinement scheme, and the need to consider frictional heat sources and dynamic effects.

References

1. Wriggers P (2006) Computational contact mechanics. Springer-Verlag, Berlin
2. Spencer BW, Williamson RL, Stafford DS, Novascone SR, Hales JD, Pastore G (2016) 3D modeling of missing pellet surface defects in BWR fuel. *Nucl Eng Des* 307:155–171
3. Williamson RL, Hales JD, Novascone SR, Tonks MR, Gaston DR, Permann CJ, Andrs D, Martineau RC (2012) Multidimensional multiphysics simulation of nuclear fuel behavior. *J Nucl Mater* 423:149–163
4. Khoei AR, Bahmani B (2018) Application of an enriched FEM technique in thermo-mechanical contact problems. *Comput Mech* 62(5):1127–1154
5. Papadopoulos P, Taylor RL (1992) A mixed formulation for the finite element solution of contact problems. *Comput Methods Appl Mech Eng* 94:373–389
6. Wriggers P, Mieke C (1994) Contact constraints within coupled thermomechanical analysis—a finite element model. *Comput Methods Appl Mech Eng* 113:301–319
7. Maday Y, Mavriplis C, Patera A (1989) Nonconforming mortar element methods: application to spectral discretizations. *Domain Decomposition Methods*, SIAM, pp 392–418
8. McDevitt TW, Laursen TA (2000) A mortar-finite element formulation for frictional contact problems. *Int J Numer Meth Eng* 48:1525–1547
9. Yang B, Laursen TA, Meng X (2005) Two dimensional mortar contact methods for large deformation frictional sliding. *Int J Numer Meth Eng* 62:1183–1225
10. Kim TY, Dolbow J, Laursen TA (2007) A mortared finite element method for frictional contact on arbitrary interfaces. *Comput Mech* 39:223–235
11. Belgacem FB, Hild P, Laborde P (1997) Approximation of the unilateral contact problem by the mortar finite element method. *Comptes Rendus de l'Academie des Sciences Series I Mathematics* 324:123–127
12. Belgacem FB, Hild P, Laborde P (1998) The mortar finite element method for contact problems. *Math Comput Model* 28:263–272
13. Puso MA, Laursen TA (2004) A mortar segment-to-segment contact method for large deformation solid mechanics. *Comput Methods Appl Mech Eng* 193:601–629
14. Yoon YC, Song JH (2014) Extended particle difference method for weak and strong discontinuity problems: part i. derivation of the extended particle derivative approximation for the representation of weak and strong discontinuities. *Computational Mechanics*, 53 (6): 1087–1103
15. Li S, Liu WK (1998) Synchronized reproducing kernel interpolant via multiple wavelet expansion. *Comput Mech* 21:28–47
16. Li S, Liu WK (1999) Reproducing kernel hierarchical partition of unity, part I-formulation and theory. *Int J Numer Meth Eng* 45:251–288
17. Li S, Liu WK (1999) Reproducing kernel hierarchical partition of unity, part I-applications. *Int J Numer Meth Eng* 45:289–317
18. Li S, Liu WK (2002) Meshfree and particle methods and their applications. *Appl Mech Rev* 55:1–34
19. Kim DW, Kim Y (2003) Point collocation method using the fast moving least-square reproducing kernel approximation. *Int J Numer Meth Eng* 56(10):1445–1464
20. Hillman M, Chen JS (2016) An accelerated, convergent, and stable nodal integration in Galerkin meshfree methods for linear and nonlinear mechanics. *Int J Numer Meth Eng* 107:603–630
21. Lee SH, Yoon YC (2004) Meshfree point collocation method for elasticity and crack problems. *Int J Numer Meth Eng* 61(1):22–48
22. Kim DW, Liu WK, Yoon YC, Belytschko T, Lee SH (2007) Mesh-free point collocation method with intrinsic enrichment for interface problems. *Comput Mech* 40:1037–1052
23. Kim DW, Yoon YC, Liu WK, Belytschko T (2007) Extrinsic meshfree approximation using asymptotic expansion for interfacial discontinuity of derivative. *J Comput Phys* 221:370–394
24. Yoon Y-C, Song J-H (2021) Interface immersed particle difference method for weak discontinuity in elliptic boundary value problems. *Comput Methods Appl Mech Eng* 375:113650
25. Yoon YC, Song JH (2014) Extended particle difference method for weak and strong discontinuity problems: part II. Formulations and applications for various interfacial singularity problems. *Comput Mech* 53(6):1105–1128
26. Yoon YC, Song JH (2014) Extended particle difference method for moving boundary problems. *Comput Mech* 54(3):723–743

27. Song JH, Fu Y, Kim TY, Yoon YC, Michopoulos JG, Rabczuk T (2018) Phase field simulations of coupled microstructure solidification problems via the strong form particle difference method. *Int J Mech Mater Des* 14:491–509
28. Fu Y, Michopoulos JG, Song JH (2017) Bridging the multi phase-field and molecular dynamics models for the solidification of nano-crystals. *J Comput Sci* 20:187–197
29. Almasi A, Beel A, Kim T-Y, Michopoulos JG, Song J-H (2019) Strong-form collocation method for solidification and mechanical analysis of polycrystalline materials. *J Eng Mech* 145(10):04019082
30. Yoon YC, Schaefferkoetter P, Rabczuk T, Song JH (2019) New strong formulation for material nonlinear problems based on the particle difference method. *Eng Anal Boundary Elem* 98:310–327
31. Almasi A, Kim T-Y, Laursen TA, Song J-H (2019) A strong form meshfree collocation method for frictional contact on a rigid obstacle. *Comput Methods Appl Mech Eng* 357:112597
32. Beel A, Kim TY, Jiang W, Song JH (2019) Strong form-based meshfree collocation method for wind-driven ocean circulation. *Comput Methods Appl Mech Eng* 351:404–421
33. Aluru NR (2000) A point collocation method based on reproducing kernel approximations. *Int J Numer Meth Eng* 47:1083–1121
34. Hu HY, Chen JS, Hu W (2011) Error analysis of collocation method based on reproducing kernel approximation. *Numer Methods Part Diff Equ* 27:554–580
35. De Lorenzis L, Evans JA, Hughes TJR, Reali A (2015) Isogeometric collocation: Neumann boundary conditions and contact. *Comput Methods Appl Mech Eng* 284:21–54
36. Kruse R, Nguyen-Thanh N, De Lorenzis L, Hughes TJR (2015) Isogeometric collocation for large deformation elasticity and frictional contact problems. *Comput Methods Appl Mech Eng* 296:73–112
37. Yeung S-K, Weeger O, Dunn ML (2017) Isogeometric collocation methods for Cosserat rods and rod structures. *Comput Methods Appl Mech Eng* 316:100–122
38. Novascone SR, Spencer BW, Hales JD, Williamson RL (2015) Evaluation of coupling approaches for thermomechanical simulations. *Nucl Eng Des* 295:910–921
39. Danowski C, Gravemeier V, Yoshihara L, Wall WA (2013) A monolithic computational approach to thermo-structure interaction. *Int J Numer Meth Eng* 95:1053–1078
40. Farhat C, Park KC, Dubois-Pelerin Y (1991) An unconditionally stable staggered algorithm for transient finite element analysis of coupled thermoelastic problems. *Comput Methods Appl Mech Eng* 85:349–365
41. Laursen TA (2003) Computational contact and impact mechanics: fundamentals of modeling interfacial phenomena in nonlinear finite element analysis. Springer-Verlag, Berlin
42. Belytschko T, Lu YY, Gu L (1994) Element-free Galerkin methods. *Int J Numer Methods Eng* 37(2):229–256
43. Geuzaine C, Remacle J-F (2009) Gmsh: a three-dimensional finite element mesh generator with built-in pre- and post-processing facilities. *Int J Numer Meth Eng* 79(11):1309–1331
44. Johnson KL (1985) Contact mechanics. Cambridge University Press, Cambridge

Publisher's Note Springer Nature remains neutral with regard to jurisdictional claims in published maps and institutional affiliations.